Petroleum Science 20 (2023) 3461–3477

Contents lists available at ScienceDirect

Petroleum Science

journal homepage: www.keaipublishing.com/en/journals/petroleum-science

Original Paper

# A transient model integrating the nanoconfinement effect and pore structure characteristics of oil transport through nanopores

Cheng Cao [a, *], Bin Chang [b, c], Zhao Yang [a], Chao Gao [d]

[a] School of Mathematics and Computer Science, Shaanxi University of Technology, Hanzhong, 723001, Shaanxi, China
[b] State Key Laboratory of Continental Dynamics, Department of Geology, Northwest University, Xi'an, 710069, Shaanxi, China
[c] Shaanxi Polytechnic Institute, Sch Civil Engn, Xianyang, 712000, Shaanxi, China
[d] Research Institute of Shanxi Yanchang Petroleum (Group) Co. Ltd, Xi'an, 710075, Shaanxi, China

ARTICLE INFO

*Article history:*
Received 4 February 2023
Received in revised form
19 July 2023
Accepted 19 July 2023
Available online 20 July 2023

Edited by Yan-Hua Sun

*Keywords:*
Nanopores
Transient transport
Nanoconfinement effect
Tortuosity
Roughness
Alkane properties

ABSTRACT

Understanding the integrated transport behavior of oil in shale nanopores is critical to efficient shale oil development. In this paper, based on the time-dependent Poiseuille flow momentum equation, we present a novel transient model to describe oil transport in unsteady and steady states. The model incorporates the effect of the critical shift density, apparent viscosity, slip length, and alkane property, as well as pore tortuosity and surface roughness. We evaluated our model through a comparison with other models, experiments, and molecular dynamics simulations. The results show that the development rates of the volume flows of $C_6$–$C_{12}$ alkane confined in inorganic nanopores and $C_{12}$ alkane confined in organic nanopores were faster than that of the corresponding bulk alkane. In addition, the critical drift density positively promoted the volume flow development rate in the unsteady state and negatively inhibited the mass flow rate in the steady state. This effect was clearest in pores with a smaller radius and lower-energy wall and in alkane with shorter chain lengths. Furthermore, both the nanoconfinement effect and pore structure determined whether the volume flow enhancement rate was greater than or less than 1. The rate increased or decreased with time and was controlled mainly by the nanoconfinement effect. Moreover, as the wall energy increased, the flow inhibition effect increased; as the carbon number of alkane increased, the flow promotion effect increased. The results indicate that the proposed model can accurately describe oil transport in shale nanopores.


## 1. Introduction

With the depletion and exhaustion of traditional oil and natural gas resources, shale oil has gradually become an important supplement and successor to traditional oil and gas. Shale, however, is a fine-grained sedimentary rock with mostly nanoscale pores (Javadpour and Ettehadtavakkol, 2015). To successfully develop oil in nanoscale shale, we must clearly understand the transport behavior of oil in nanoscale pores. Oil transport in nanoscale pores is affected by many factors, including the properties of confined oil deflecting from bulk oil and slip effects, which are common physical phenomena in nanopores (Tao et al., 2020). Thus, oil transport in nanopores is completely different from that in sandstone. In addition, the main components of oil are alkanes, and each component has a different transport capacity in nanopores. Furthermore, the pores in the shale matrix are generally curved, and the inner surfaces of the pores are rough and uneven, which can affect the oil transport efficiency in shale nanopores. Finally, shale oil development is often accompanied by the commissioning of new wells, the rehabilitation of damaged wells, and the intermittent production of low-producing wells, leading to the transient behavior of oil transport in nanopores. Therefore, a comprehensive understanding of the effects of different factors on the transient transport characteristics of oil in shale nanopores is necessary to achieve high-quality shale oil development.

Liquids in large pores are considered to be similar to bulk liquids. The properties of liquids in nanoscale pores, however, vastly differ from those of bulk liquids and are thus regarded as confined liquids (Thomas and McGaughey, 2008). In large pores, the effect of the interaction between the pore wall and the liquid on the

* Corresponding author.
*E-mail address:* caocheng@snut.edu.cn (C. Cao).

https://doi.org/10.1016/j.petsci.2023.07.015

properties of the liquid occurs within a thin layer near the wall, and the effect of the fluid properties within this layer on the properties of the liquid in the entire nanopore can be negligible. In nanopores, because the pore radius is so small, this layer accounts for a large proportion of the entire pore area, making its influence on the fluid properties in the nanopore significant (Sendner et al., 2009; Zhang et al., 2020) and worthy of attention. Many researchers have studied fluid properties in nanopores through experiments (Majumder et al., 2005; Holt et al., 2006; Secchi et al., 2016) and molecular dynamics simulations (Cao et al., 2006; Argyris et al., 2011; Podolska and Zhmakin, 2013; Li et al., 2015; Qiu et al., 2015; Kobayashi et al., 2016; Tao et al., 2020). The results indicate that the internal structure of the liquid molecules, as well as the arrangement between the molecules in the region close to the pore wall, significantly differs from that of the bulk liquid (liquid in the central region of the nanopore or in the macropore). As the liquid moves away from the pore wall, the effect of the wall on the liquid molecules gradually decreases, and the internal structure of the liquid molecules and the arrangement between molecules gradually become more similar to those of the bulk liquid. This causes radial inhomogeneity of liquid properties in nanopores and also leads to slip (Wang et al., 2016; Yang et al., 2017; Zhang et al., 2019a). Many scholars have studied the transport characteristics of liquids under mesoscopic conditions by applying viscosity and slip corrections to the Hagen–Poiseuille (HP) equation. Some scholars have also studied the liquid flow in single nanopores. For example, Thomas and McGaughey (2009), Myers (2011), and Wu et al. (2017) proposed flow enhancement factors to describe the difference in flow between confined liquid and bulk liquid. The flow enhancement factors they proposed are similar in form and are defined by the slip length, pore radius, and ratio of the bulk liquid viscosity to the effective viscosity. The differences lie in the expressions for the slip length and effective viscosity. Ma et al. (2011) proposed a slip-length model considering the dynamic friction coefficient to study the fluid transport in nanopores. Further, Mattia and Calabrò (2012) introduced viscous effects and surface diffusion into the flow enhancement factor. Shaat and Zheng (2019) and Wu et al. (2021) further considered the effect of the radial inhomogeneous distribution of viscosity on the velocity profile and proposed a flow enhancement factor closer to the actual situation. Cui (2019) investigated the effect of mixed wetness, asphaltene, and viscosity enhancement on the flow enhancement factor in shale oil reservoirs. Wang et al. (2019a) further studied the flow enhancement factor in elliptical-shaped nanopores. Other scholars have studied the transport behavior of liquid in porous media shale. For example, Wang et al. (2019b) considered the elliptical nanopore and the difference in liquid transport in organic and inorganic nanopores to establish an apparent liquid permeability model. Feng et al. (2019) studied the difference in liquid transport in nanopores and nanoscale fractures and established an apparent liquid permeability model considering the inhomogeneous distribution of pore size.

Undoubtedly, the aforementioned studies have improved our understanding of liquid transport in nanopores. However, their main research focus was on the effect of liquid viscosity and slip length on liquid transport caused by nanoconfinement effects, not on nanoconfinement effects, which can cause the liquid density to deviate from that of bulk liquid. For example, the interaction between the wall and the liquid leads to a drift in the critical temperature of the confined liquid (Feng et al., 2020, 2021), which changes the density of the confined liquid. Therefore, if the flow enhancement factor derived based on the steady-state HP equation is used to describe the transport behavior of the liquid in the nanopore, the effect of critical density drift will be neglected. In Eq. (1), for example, no density item exists in the steady-state HP equation:

$$Q = \frac{\pi R^4 \Delta \boldsymbol{p}}{8\mu L}, \tag{1}$$

where $Q$ is the volumetric flux, $m^3/s$; $R$ is the pore radius, m; $\Delta \boldsymbol{p}$ is the pressure difference, Pa; $\mu$ is the liquid viscosity, Pa s; $L$ is the length of the pore, m. In addition, when the density and viscosity of the confined liquid in the nanopore deviate from the bulk liquid, the inertial force and internal friction of the liquid will change significantly, and the slip effect will also change the liquid movement rate near the pore wall. These factors will affect the fluid development rate in the nanopore—that is, the transport behavior of the liquid in the unsteady state. However, the steady-state HP equation cannot be used to describe the transport behavior of the liquid in the unsteady state.

Furthermore, the pore structure (i.e., tortuosity and roughness) greatly influences oil transport in nanopores (Liu et al., 2021; Tian et al., 2022). However, characterizing the roughness and tortuosity requires a large number of parameters that are not easily obtained (Jin et al., 2017; Zeng et al., 2018; Lee and Babadagli, 2021), making it difficult to study the flow behavior of liquids in tortuous and rough pores. Fortunately, fractal theory is a good approach for such a study, with few parameters involved and a clear physical meaning. Research combining fractal theory and fluid transport has also made progress. For example, Wang and Cheng (2019) studied the transport behavior of water in the shale matrix by fractal theory, considering the effect of wall wettability on fluid properties and the fractal characteristics of pore size and tortuosity. They then established an apparent fluid permeability model for shale. Fan et al. (2020) used fractal theory to establish the essential permeability of shale, considering surface roughness and tortuosity. They combined it with the flow enhancement factor to propose an apparent permeability model. Li et al. (2020) and Miao et al. (2015) studied the relative permeability model of gas and water phases in fractures by fractal theory. The transient transport of oil in nanopores, however, has been less studied according to fractal theory.

In conclusion, the transport behavior of oil in shale pores is affected by a combination of many factors, but no study has been done on the combined effect of the nanoconfinement effect and pore structure on the transient transport behavior of oil of different compositions in nanopores. Therefore, the development of a transient model to study the integrated transport behavior of oil in nanopores is urgently needed.

The objective of this study was to develop a transient model that can synthetically describe oil transport in nanopores to elucidate the effects of nanoconfinement effects and pore structure on oil transport behavior of in the unsteady and steady states. First, we converted the time-dependent momentum equation of Poiseuille flow into a second-order ordinary differential equation with variable coefficients by Laplace transformation, and then we solved this equation with Bessel functions to obtain the time-dependent velocity solution in Laplace space. The drift density model, the apparent viscosity model, the slip model, and the fractal model characterizing the tortuosity and relative roughness were also established. The established transient velocity equation was modified by these models to obtain a transient model considering the effects of nanoconfinement effects and pore structure. The plausibility of the proposed models was verified by a comparison with other models, as well as experimental and molecular dynamics (MD) simulations. The transport characteristics of different alkanes in organic and inorganic pores were modeled, and the unsteady and steady transport behavior were assessed. This model offers an important complement to the steady transport of confined liquid in nanopores. In addition, the oil–gas two-phase transport in shale nanopores involves the mass exchange of oil and gas, which

must be studied according to transient models. Our proposed model establishes a foundation for an analytical model of oil–gas two-phase flow in shale pores.

## 2. Methods

### 2.1. Establishment of a transient transport model

For constant pressure boundary conditions, the fluid velocity varies continuously with time in the unsteady state and stops changing after reaching the steady state. Because of the influence of the boundary layer, the fluid velocity distribution gradually transitions from the segment plug type to the parabolic type (Fig. 1).

Unsteady flow can be described by the Navier–Stokes (N–S) equation. The condition for the applicability of the equation is the continuous medium assumption, which is valid when it is applied to macroscopic fluid flow. This assumption requires that the volume of the molecular cluster (fluid mass) be infinitely small at the macroscopic level, and it can be viewed as a collection of points with no spatial dimensions. Despite being infinitely large at the microscopic level, the molecular cluster must include a large number of liquid molecules, and a few molecules entering and leaving the cluster do not affect the stable average value. However, for nanoscale fluid domains, the continuous medium assumption may not be valid. For gas confined in nanopores, the Knudsen number ($Kn$) is a key parameter that can be used to determine whether the continuous medium assumption condition holds. For example, when $Kn < 0.001$, it is a continuous flow; thus, the continuous medium assumption condition holds, and the N–S equation applies. When $0.001 < Kn < 0.1$, it is a slip flow, and the N–S equation combined with the slip boundary condition is applicable. When $Kn > 0.1$, it is transitional flow; when $Kn > 10$, it is free molecular flow. The N–S equation is inapplicable when the gas flow mechanism is a transition flow and free molecular flow (Li et al., 2018; Wang and Aryana, 2021; Rustamov et al., 2023). For liquids, since the mean free path of liquid molecules is much smaller than that of gas molecules, $Kn$ is used to determine the flow mechanism of liquid, and correcting the liquid flow equation can cause some deviation (Zhang et al., 2019b). However, the definition of the continuous medium assumption condition can be used. For example, if decane ($C_{12}H_{26}$) flows in a pore with a radius of 5 nm, the length of the fluid microcluster should be at least 1 nm, and only 3.12 molecules are included in a fluid microcluster of 1 $nm^3$. Thus, the continuous medium assumption cannot be satisfied. Even so, the N–S equation with a slip boundary and viscosity correction can still obtain good results for liquid in nanopores. Several studies (Feng et al., 2019; Wang et al., 2019c; Cui, 2019; Zhang et al., 2019b) have shown that the HP equation (the simplified solution of the N–S equation) corrected by slip and viscosity is suitable for modeling the nanoscale flow of liquids, indicating that the corrected N–S equation can be used for describing liquid flow in nanopores. To introduce the time item, we use the time-dependent N–S equation to describe the flow of liquids in nanopores, assuming that the pores of a constant cross section placed horizontally neglect gravity and that the pressure gradient is constant. Considering these factors, we simplify the N–S equation in the cylindrical coordinate system into the following form:

$$\frac{\partial^2 \boldsymbol{u}}{\partial r^2}+\frac{1}{r}\frac{\partial \boldsymbol{u}}{\partial r}-\frac{\rho}{\mu}\frac{\partial \boldsymbol{u}}{\partial t}=-\frac{\Delta \boldsymbol{p}}{\mu L}, \tag{2}$$

where $\boldsymbol{u}$ is the liquid flow velocity, m/s; $r$ is the radial distance from the center of the pore, m; $\rho$ is the density of the liquid, $kg/m^3$. The third term on the left side of Eq. (2) is the transient item. The initial and boundary conditions are given by the following equation:

$$\boldsymbol{u}\left(r,0\right)=0,\ \ \boldsymbol{u}\left(R,t\right)=l_s\frac{\partial \boldsymbol{u}}{\partial r},\ \ \boldsymbol{u}\left(0,t\right)=\text{finite}, \tag{3}$$

where $l_s$ is the liquid slip length, m; Transforming Eq. (3) into the Laplace space and combining initial conditions, we can obtain

$$\frac{\partial^2 \boldsymbol{U}}{\partial r^2}+\frac{1}{r}\frac{\partial \boldsymbol{U}}{\partial r}-\frac{\rho}{\mu}s\boldsymbol{U}=-\frac{\Delta \boldsymbol{p}}{\mu L \boldsymbol{s}}, \tag{4}$$

where $\boldsymbol{U}$ denotes the liquid flow velocity in Laplace space; and $\boldsymbol{s}$ is the Laplace space variable. Eq. (4) is a nonhomogeneous differential equation with a variable coefficient, and its special solution is as follows:

$$\boldsymbol{U}=\frac{1}{\rho \boldsymbol{s}^2}\frac{\Delta \boldsymbol{p}}{L}. \tag{5}$$

The corresponding homogeneous equation of Eq. (4) is given as follows:

$$\frac{\partial^2 \boldsymbol{U}}{\partial r^2}+\frac{1}{r}\frac{\partial \boldsymbol{U}}{\partial r}-\frac{\rho}{\mu}\boldsymbol{s}\boldsymbol{U}=0. \tag{6}$$

Eq. (6) is a Bessel equation of an imaginary argument, and its general solution is given as follows:

$$\boldsymbol{U}=C_1 I_0\left(\sqrt{\frac{\rho \boldsymbol{s}}{\mu}}r\right)+C_2 K_0\left(\sqrt{\frac{\rho \boldsymbol{s}}{\mu}}r\right), \tag{7}$$

where $C_1$ and $C_2$ are the undetermined coefficients, dimensionless; $I_0$ and $K_0$ are the zero-order Bessel function of the imaginary

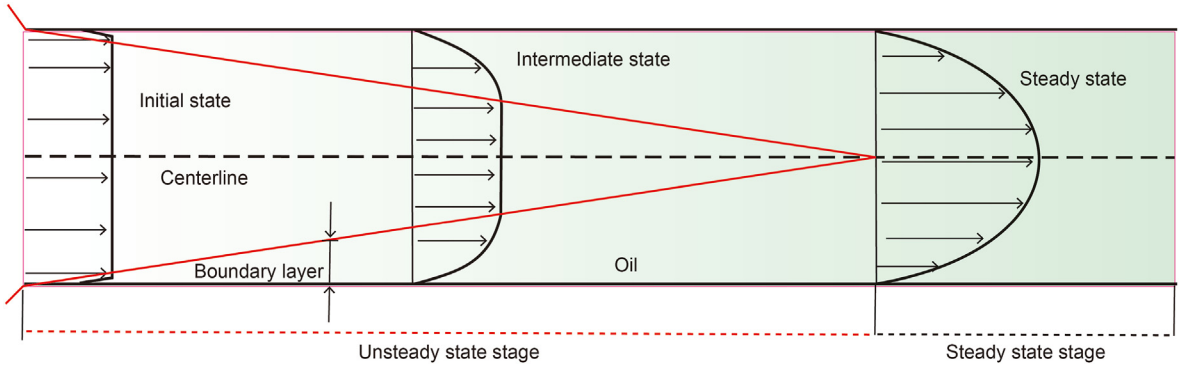


**Fig. 1.** Schematic diagram of transient flow.

argument of the first and second kinds, respectively.

Combining Eq. (5) and Eq. (7), we can obtain the general solution of Eq. (4):

$$\boldsymbol{U} = C_1 I_0\left(\sqrt{\frac{\rho \boldsymbol{s}}{\mu}} r\right) + C_2 K_0\left(\sqrt{\frac{\rho \boldsymbol{s}}{\mu}} r\right) + \frac{1}{\rho \boldsymbol{s}^2}\frac{\Delta \boldsymbol{p}}{L}. \tag{8}$$

Substituting the initial and boundary conditions, we can obtain $C_1$ and $C_2$, respectively, as

$$C_1 = -\frac{\frac{1}{\rho \boldsymbol{s}^2}\frac{\Delta \boldsymbol{p}}{L}}{l_s\sqrt{\frac{\rho \boldsymbol{s}}{\mu}} I_1\left(\sqrt{\frac{\rho \boldsymbol{s}}{\mu}} R\right) + I_0\left(\sqrt{\frac{\rho \boldsymbol{s}}{\mu}} R\right)}, \quad C_2 = 0, \tag{9}$$

where $I_1$ is the one-order Bessel function of the imaginary argument of the first kind. Substituting Eq. (9) into Eq. (8), we obtain the transient flow model considering slip:

$$\boldsymbol{U}(r,t) = \frac{1}{\rho \boldsymbol{s}^2}\frac{\Delta \boldsymbol{p}}{L_0}\left[1 - \frac{I_0\left(\sqrt{\frac{\rho \boldsymbol{s}}{\mu}} r\right)}{I_0\left(\sqrt{\frac{\rho \boldsymbol{s}}{\mu}} R\right) + l_s\sqrt{\frac{\rho \boldsymbol{s}}{\mu}} I_1\left(\sqrt{\frac{\rho \boldsymbol{s}}{\mu}} R\right)}\right]. \tag{10}$$

### 2.2. Modeling of nanoconfinement effects

#### 2.2.1. Establishment of the critical drift density model

The critical properties of the liquid confined in the nanopore are completely different from those of the corresponding bulk liquid, including critical temperature. The shift from the critical temperature of the bulk liquid is caused by the interaction between the pore wall and the liquid and pore dimensions. Tan et al. (2020) proposed the critical drift temperature model as follows:

$$\Delta T_c = 1 - \frac{T_c}{T_{cb}} = \lambda\frac{1}{m} + o\left(\lambda\frac{1}{m}\right)^3, \tag{11}$$

where $\Delta T_c$ and $T_c$ are the critical drift temperature and the critical temperature of confined liquid, K, respectively; $T_{cb}$ is the critical temperature of the bulk liquid, K; $\lambda$ is the proportional relationship between the wall–liquid interaction and the liquid–liquid interaction, dimensionless. When $\lambda$ is 1, $\Delta T_c$ and $T_c$ are equal. $M$ is the pore dimension, dimensionless, and it is equal to the ratio of the pore radius $R$ to the LJ size parameter ($\sigma$). In general, when the pore radius is greater than 1 nm, the small amount of the third order of the second term on the right side of the equation can be neglected. The pore radius in the range we studied was greater than 1 nm, so it was neglected. The relationship between $\lambda$ and the contact angle characterizing the macroscopic wettability can be given as follows (Zhao et al., 2017):

$$\lambda = -\frac{0.6\ln(\theta/180)}{\eta}, \tag{12}$$

where $\theta$ is the contact angle, degree; $\eta$ is the correction factor, dimensionless, which is generally taken as 0.56 in a circular hole. The critical temperature of the confined liquid can be obtained by combining Eq. (11) and Eq. (12):

$$T_c = T_{cb}\left[1 - 0.6\cdot\eta\ln\left(\frac{180}{\theta}\right)\frac{1}{m}\right], \tag{13}$$

where the contact angle can be determined by Young's equation (see Section 2.2.3). The critical temperature of the confined liquid drifted relative to the bulk liquid, resulting in a change in the number of molecules per unit volume. Therefore, the density of the confining liquid also drifted relative to the bulk liquid (Feng et al., 2021). We use the critical drift density to represent the density of liquid confined in the nanopore and obtain it by using the following correlations (Chouaieb et al., 2004):

$$\ln\left(\rho_r\right) = \alpha\left\{1 + (1 - T/T_c)^b - \exp\left[-(1 - T/T_c)^b\right]\right\}, \tag{14}$$

with

$$\rho_r = \rho_{shift}\big/\rho_c, \tag{15}$$

where $\rho_r$ is the reduced density, dimensionless; $\rho_{shift}$ is the critical drift density of confined liquid, kg/m$^3$; $\rho_c$ is the critical density of the bulk liquid, kg/m$^3$; and $a$ and $b$ are the fitting coefficients, dimensionless. By combining Eqs. (12)–(15), we can obtain the critical drift density model as follows:

$$\rho_{shift} = \rho_c \exp\langle a\left\{1 + \left(1 - \frac{T}{T_c}\right)^b - \exp\left[-\left(1 - \frac{T}{T_c}\right)^b\right]\right\}\rangle. \tag{16}$$

From Eq. (16), it can be seen that the critical drift density is a function of $T_c$, where $T_c$ is a function of the critical temperature ($T_{cb}$), the contact angle ($\theta$), and the pore dimension ($m$), which together control the critical drift density. Fig. 2(a) shows the variation of $\rho_{shift}/\rho_b$ with $m$ as well as the contact angle. The deviation of $\rho_{shift}/\rho_b$ from 1 increases with a decreasing $m$ and contact angle, indicating a larger density shift for smaller pore dimensions and stronger wettability. Fig. 2(b) shows that the sensitivity of $C_{12}$ (dodecane) to pore dimension and contact angle decreases because of the increase in the critical temperature of alkanes with the increasing carbon number, leading to a weaker nanoconfinement effect.

#### 2.2.2. Establishment of the apparent viscosity model

The wall–liquid interaction in the relaxation time of the liquid in the wall region deviates from that of the bulk liquid. In the center of the pore, the liquid relaxation time is equal to that of the bulk liquid. In addition, the relaxation time is related to the wall energy (see Section 2.2.3 for details of "wall energy") and the type of liquid. Wu et al. (2019) obtained the reduced relaxation time of different alkanes by molecular simulation. Fig. 3 shows that the reduced relaxation time of alkanes increases with the increasing wall energy ($\sigma_s^d$) and alkane carbon number. Farrer and Fourkas (2003) proposed a relationship between the relaxation time and viscosity of the liquid:

$$\frac{\mu_i}{\mu_b} = \frac{\tau_i}{\tau_b}, \tag{17}$$

where $\mu_i$ and $\tau_i$ denote the viscosity and relaxation time of the liquid in the wall region, respectively, Pa s and s. The thickness of the wall region is approximately the thickness of one molecular layer $\delta$, m; $\mu_b$ and $\tau_b$ denote the viscosity and relaxation time of the bulk liquid, Pa s and s, respectively. The apparent viscosity can be obtained by weighing the area:

$$\mu_{app} = \mu_b\left[\frac{\tau_i}{\tau_b}\frac{A_i}{A_t} + \left(1 - \frac{A_i}{A_t}\right)\right], \tag{18}$$

where $\mu_{app}$ is the apparent viscosity of the confined liquid, Pa s; $A_i$ and $A_t$ are the cross-sectional areas of the wall region and the total cross-sectional area of the pore, m$^2$, respectively, as shown in Fig. 4.

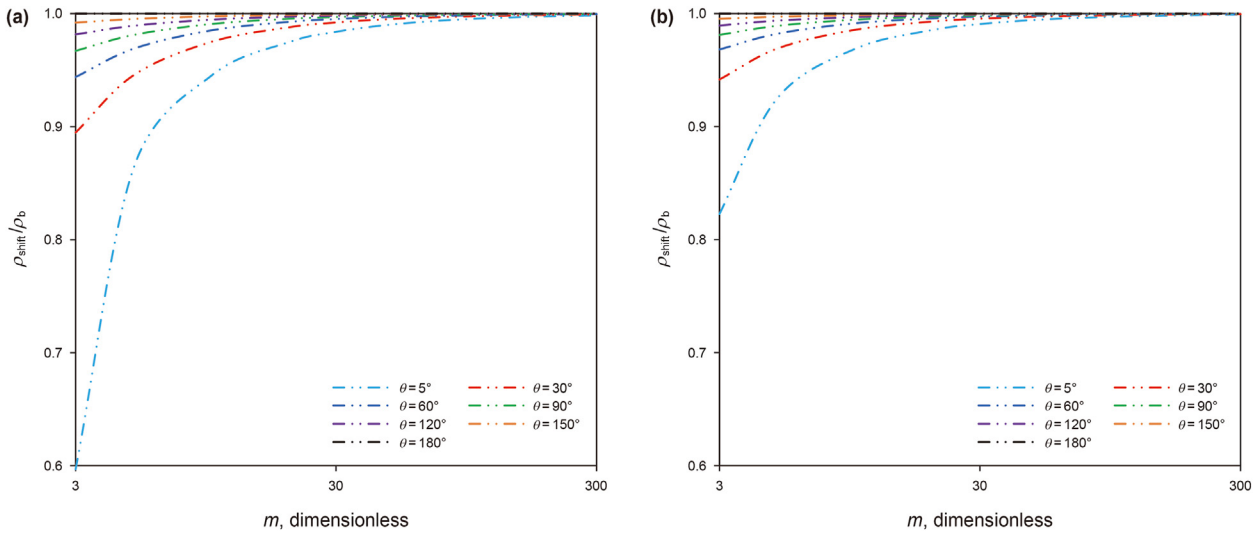


**Fig. 2.** Variation of $\rho_{shift}/\rho_{no\text{-}shift}$ with $m$ ($T = 293.15$ K). (**a**) $C_6$ (hexane); (**b**) $C_{12}$ (dodecane).

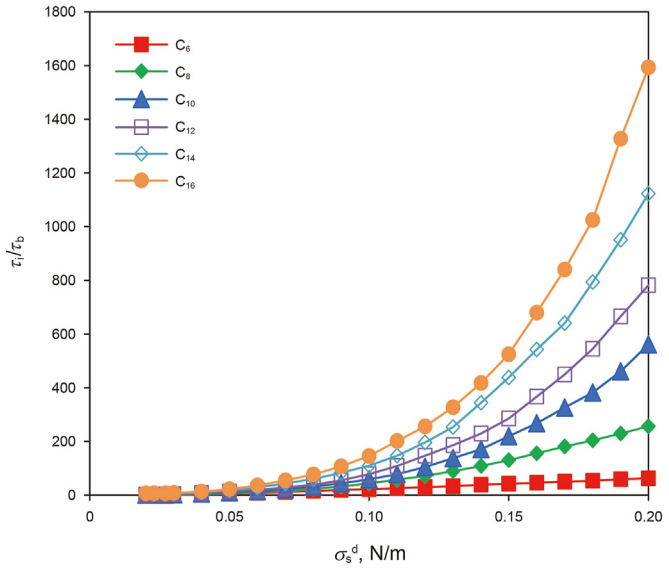


**Fig. 3.** Variation of $\tau_i/\tau_b$ with $\sigma_s^d$.

### 2.2.3. Establishment of the slip length model

The slip occurs mainly in the depletion layer (Myers, 2011; Shaat and Zheng, 2019). The liquid molecules in the depletion layer are mainly affected by the electrostatic repulsive forces, which may be the reason for the slip occurrence. In addition, the liquid–wall interaction affects the slippage of the liquid molecules. When the interaction is strong, the friction between the wall and liquid is large, and the slip effects are weakened or even negligible, and vice versa. The wall–liquid interaction is controlled by both the contact angle and the reduced relaxation time of liquid (Wu et al., 2019). For a high-energy wall, the liquid vapor will adsorb on the wall, resulting in a larger contact angle and reduced relaxation time. Combining these two factors, we can see that as the wall energy decreases, the liquid–wall interaction weakens; and vice versa, as Fig. 5 shows.

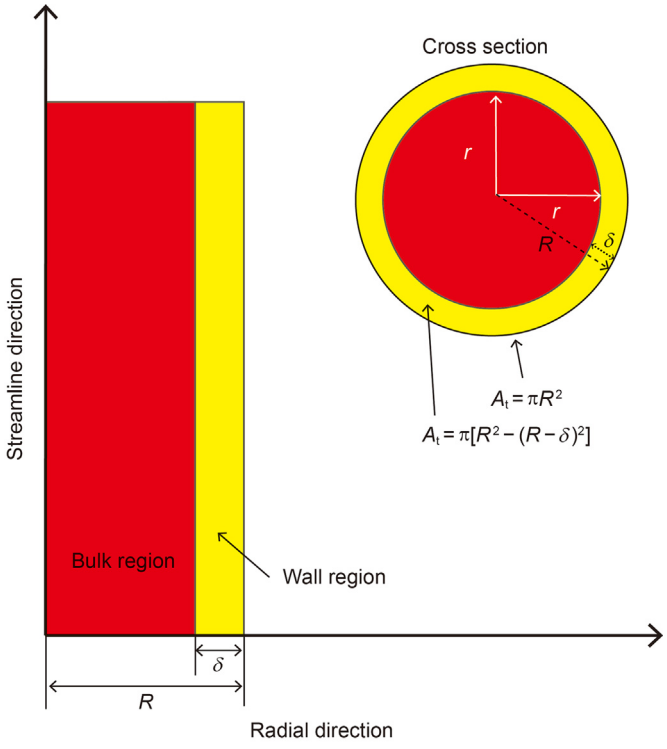


**Fig. 4.** Schematic diagram of wall region and bulk region.

The slip length can be expressed as the ratio of the velocity of movement of the first molecular layer closest to the pore wall to that of the remaining molecular layer (Blake, 1990):

$$l_s = \delta\left(\frac{\eta_i}{\eta_b} - 1\right), \tag{19}$$

where $\delta$ is the thickness of a single molecular layer, m; and $\eta_i$ and $\eta_b$ are the movement velocities of the first molecular layer and the

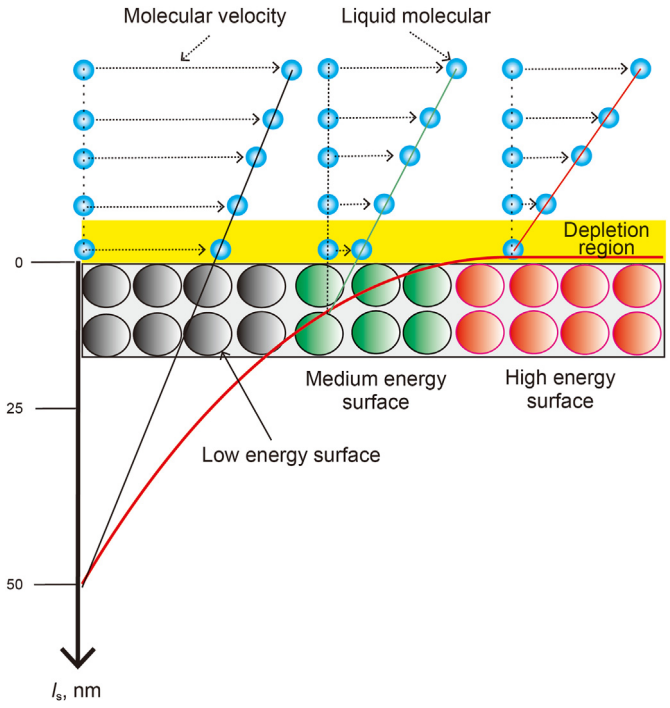


**Fig. 5.** Schematic diagram of slip. The thicker red line represents the variation of the slip length with the wall energy. The first layer of liquid molecules adjacent to the high-energy wall move a short distance, indicating that the slip length is almost negligible; as the wall energy increases, the first layer of liquid molecules moves an increased distance, indicating that the slip length increases.

remaining molecular layer, respectively, m/s. The ratio of the two can be expressed by the following equation (Wu et al., 2019):

$$\frac{\eta_i}{\eta_b}=\frac{\tau_b}{\tau_i}\exp\left\{\frac{\pi[0.1265)(n-1)+0.46]^2}{6kT}\sigma_l(1-\cos\theta)\right\}, \tag{20}$$

where $n$ is the carbon number of the alkane, dimensionless; $\sigma_l$ is the liquid surface free energy, N/m; $k$ is the Boltzmann constant, $1.38\times10^{-23}$ J/K; $T$ is the temperature, K. $\cos\theta$ can be calculated by the modified Young's equation (Fowkes, 1964):

$$\cos\theta=-1+2\zeta\sqrt{\frac{\sigma_s^d}{\sigma_l^d}}-\frac{\pi_e}{\sigma_l}, \tag{21}$$

where $\zeta$ is the characteristic constant, dimensionless, which is generally less than 1 for inhomogeneous molecular structures. Hydrocarbon liquids belong to inhomogeneous molecular structures, so they are taken as 0.85; $\sigma_s^d$, $\sigma_l^d$ are the contributions of dispersion forces to the pore wall free energy and liquid surface free energy, respectively, N/m. We studied hydrocarbon alkanes, which have strong structural inhomogeneity, so we neglected the contribution of polar forces to the liquid surface free energy, that is, $\sigma_l=\sigma_l^d$ (Marmur, 2006). $\pi_e$ represents the equilibrium diffusion pressure, N/m; when the high-energy wall and low-energy liquid interact, the vapor of the liquid forms a thin film on the wall, reducing the wall–liquid interaction. This can be calculated by the following equation (Fowkes et al., 1980):

$$\frac{\pi_e}{\sigma_l}=2\sqrt{\frac{\sigma_s^d}{\sigma_l}}-2. \tag{22}$$

Substituting Eq. (22) into Eq. (21), we can obtain the contact angle corrected by the equilibrium diffusion pressure as follows:

$$\theta=\arccos\left[1+2(\zeta-1)\sqrt{\frac{\sigma_s^d}{\sigma_l}}\right]\cdot\frac{180}{\pi}. \tag{23}$$

Eq. (23) can be used for the calculation of the contact angle given in Section 2.2.1. Substituting Eqs. (19)–(23) into Eq. (18), we obtain the slip length model:

$$l_s=\delta\langle\frac{\tau_b}{\tau_i}\exp\left\{\frac{\pi[0.1265)(n-1)+0.46]^2}{6kT}\sigma_l\left[2(1-\zeta)\sqrt{\frac{\sigma_s^d}{\sigma_l}}\right]\right\}-1\rangle. \tag{24}$$

Note that the contribution of dispersion forces to the pore wall free energy ( $\sigma_s^d$ ) is the key parameter determining the slip length. Moreover, the reduced relaxation time, which is used to determine the apparent viscosity, is also closely related to $\sigma_s^d$. For convenience, we refer to "wall energy" instead of "contributions of dispersion forces to the pore wall free energy" in this paper.

### 2.3. Establishment of the pore structure model

The real length $L_t$ of pores in shale porous media is much longer than its apparent linear length ($L_s$), as Fig. 6 shows, causing flow direction separation. In addition, the inner surfaces of true pores are uneven, causing the fluid to generate eddy currents. Eddy currents also cause flow direction separation. Therefore, the flow resistance of the fluid in the tortuous and surface roughness of the pore also increases significantly. Both the real length of pores and surface roughness follow fractal characteristics (Yang et al., 2014, 2015a), so we used fractal theory to establish the pore structure model.

#### 2.3.1. Establishment of real pore length model

The real length of the pores obeys the fractal law and is a function of pore radius (Yang et al., 2014):

$$L_t(R)=(2R)^{1-D_t}L_s^{D_t}, \tag{25}$$

where $L_t$ is the real length of the pore, m; $L_s$ is the equivalent linear length of the pore, m; and $D_t$ is the fractal dimension of tortuosity, dimensionless, which ranges from 1 to 3. When $D_t$ is 1, the pore is straight, and when it is greater than 1, the pore is curved. The fractal dimension ($D_t$) can be obtained by the following equation (Yang et al., 2014):

$$D_t=1+\frac{\ln\tau_{ave}}{\ln[L_s/(2R_{ave})]}, \tag{26}$$

where $\tau_{ave}$ is the average tortuosity of porous media; and $R_{ave}$ is the average pore radius of porous media, m.

#### 2.3.2. Establishment of relative roughness model

The rough surface of a pore can be characterized by multiple cones (rough elements) of different sizes, as Fig. 6 shows. The relative roughness of a cylindrical pore can be represented by the following fractal function (Chen et al., 2015):

$$\varepsilon=\frac{h_{ave}}{R}=\frac{\varphi(h_{max})_{R_{pmin}}}{3R_{pmin}}\frac{2-D_c}{3-D_c}\frac{1-\beta^{3-D_c}}{1-\varphi}, \tag{27}$$

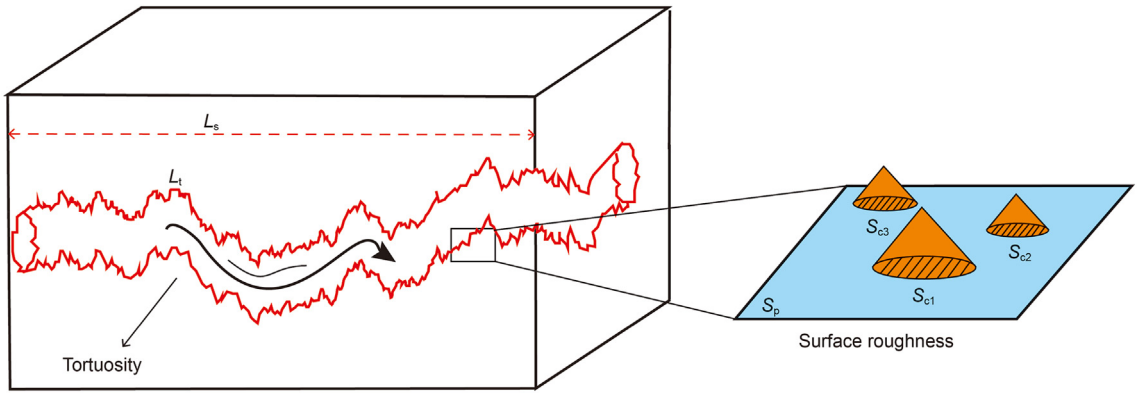


**Fig. 6.** Schematic diagram of the real length and the roughness of the pore wall, where $S_c$ is the base area of each cone, and $S_p$ is the area of the inner surface of the pore.

where $\varepsilon$ is the relative roughness, dimensionless; $h_{ave}$ is the average height of the cone, m; and $\varphi$ is the ratio of the sum of the base area of the cone to the total pore surface area, dimensionless. As Fig. 5 shows, the sum of the base areas of the cone is $S_{c1} + S_{c2} + S_{c2}$. The larger the value of $\varphi$, the larger the proportion of the unsmooth surface to the total pore surface, indicating the larger relative roughness. Moreover, $(h_{max})_{R_{pmin}}$ is the maximum cone height at the minimum pore radius, m; $R_{pmin}$ is the minimum pore radius, m; and $\beta$ is the ratio of the minimum base diameter to the maximum base diameter, dimensionless. The volume of the cone is $\pi d^3\beta/3$, where $d$ is the base diameter of a cone, indicating that the larger the value of $\beta$, the larger the volume of the cone, meaning that the relative roughness is also larger. $D_c$ can be calculated by the following equation:

$$D_c = 2 - \frac{\ln\varphi}{\ln\beta}, \tag{28}$$

where $D_c$ is the fractal dimension of the cone base size distribution, dimensionless. The range of $D_c$ is 0–2. When $D_c$ is 0, the surface of the pore is all smooth, and when $D_c$ reaches 2, the surface of the pore is not smooth.

### 2.4. Establishment of the mathematical model of liquid transport in nanopores

Substituting Eqs. (16), (18), (24) and (25) into Eq. (10) and further combining Eq. (27), we obtain the liquid transient velocity profile model considering the pore structure characteristics and nanoconfinement effect:

$$\boldsymbol{U}_{app}(R,t) = \frac{1}{\rho_{shift}\boldsymbol{s}^2}\left[1 - \frac{I_0\left(\sqrt{\frac{\rho_{shift}\boldsymbol{s}}{\mu_{app}}}r\right)}{I_0\left(\sqrt{\frac{\rho_{shift}\boldsymbol{s}}{\mu_{app}}}R(1-\varepsilon)\right) + l_s\sqrt{\frac{\rho_{shift}\boldsymbol{s}}{\mu_{app}}}I_1\left(\sqrt{\frac{\rho_{shift}\boldsymbol{s}}{\mu_{app}}}R(1-\varepsilon)\right)}\right]\frac{\Delta\boldsymbol{p}}{(2R)^{1-D_t}L_s{}^{D_t}}. \tag{29}$$

Integrating Eq. (29) from 0 to $R(1-\varepsilon)$ yields the corresponding volumetric flux model:

$$Q(R,t) = \frac{\pi}{\rho_{shift}\boldsymbol{s}^2}\left[R^2(1-\varepsilon)^2 - \frac{2R(1-\varepsilon)\sqrt{\frac{\mu_{app}}{\rho_{shift}\boldsymbol{s}}}I_1\left(\sqrt{\frac{\rho_{shift}\boldsymbol{s}}{\mu_{app}}}R(1-\varepsilon)\right)}{I_0\left(\sqrt{\frac{\rho_{shift}\boldsymbol{s}}{\mu_{app}}}R(1-\varepsilon)\right) + l_s\sqrt{\frac{\rho_{shift}\boldsymbol{s}}{\mu_{app}}}I_1\left(\sqrt{\frac{\rho_{shift}\boldsymbol{s}}{\mu_{app}}}R(1-\varepsilon)\right)}\right]\frac{\Delta\boldsymbol{p}}{(2R)^{1-D_t}L_s{}^{D_t}}, \tag{30}$$

where $Q(R,t)$ is the volumetric flux in the Laplace space, and Eq. (30) can be calculated by numerical inversion. If the effect of nanoconfinement effects and pore structure is neglected, then $\rho_{shift}$ and $\mu_{app}$ will be reduced to $\rho_b$ and $\mu_b$, respectively; $l_s$ and $\varepsilon$ will degenerate to 0; and $D_t$ will change to 1. Eq. (30) is transformed into a transient equation describing the transport of a bulk liquid in a straight and smooth pore:

$$Q_{no-slip}(R,t) = \frac{\pi}{\rho_b\boldsymbol{s}^2}\left[R^2 - \frac{2R\sqrt{\frac{\mu_b}{\rho_b\boldsymbol{s}}}I_1\left(\sqrt{\frac{\rho_b\boldsymbol{s}}{\mu_b}}R\right)}{I_0\left(\sqrt{\frac{\rho_b\boldsymbol{s}}{\mu_b}}R\right)}\right]\frac{\Delta\boldsymbol{p}}{L_s}. \tag{31}$$

To clearly understand the effect of pore structure and nanoconfinement effects on liquid transport, we define the transient volume flow enhancement rate of liquid as follows:

$$\psi_v(t) = \frac{Q(R,t)}{Q_{no-slip}(R,t)}. \tag{32}$$

### 2.5. Model limitations

Our critical shift density and apparent viscosity model are homogeneous in the radial direction of the pore. Because the real density and viscosity distribution in the nanopore are inhomogeneous, they are functions of the distance from the center of the pore. The momentum equation will be difficult to solve analytically if the inhomogeneous density and viscosity are introduced into the time-dependent Poiseuille flow momentum equation. In addition, the tortuosity and surface roughness of the pores can cause the separation of flows, resulting in nonlinear pressure gradients and creating difficulties in solving the momentum equation. Therefore, in future work, we will use the numerical method to solve these problems.

## 3. Model validation and comparison

### 3.1. Validation of velocity profile with a general transient model and the HP model

Eq. (10) is a key model that determines the correctness of the subsequent model in Eq. (30), so we first verified its correctness. We compared the proposed velocity profile model (Eq. (10)) with the Papanastasiou model (Papanastasiou et al., 1999) and the steady-state HP flow model. The data used in Eq. (10) were as follows: liquid density of 1000 kg/m$^3$, viscosity of 0.001 Pa s, pore radius of 200 nm, and pressure gradient of $1 \times 10^{11}$ Pa/m. The results are shown in Fig. 7(a). The results of our proposed model, in Eq. (10), align with those of the Papanastasiou model at each time point, and the results at 10 ns (when the flow reached a steady state) are also consistent with those of the steady-state HP model. These results indicate that our model can be used to accurately describe the unsteady transport behavior of liquid.

### 3.2. Validation of volume flow enhancement rate with MDS and experiment

We used the results of Eq. (32) at a time of 100 ps (for nanoscale pores, the flow of liquid can reach steady at 100 ps) to verify the credibility of the steady transport by comparing them with the experimental and molecular simulation results in the literature. We collected a total of 13 experimental data points and 64 molecular simulation data points, as Table S1 in Supplementary data shows. The comparison results are shown in Fig. 7(b). Most of the results obtained from our proposed model align well with the experimental and molecular simulation results in the literature, indicating that the proposed model accurately reflects the influence of microphysical phenomena on macroscopic liquid transport behavior. The effects of roughness and tortuosity on the experimental and molecular simulation results have not been reported in most prior research. Because perfectly smooth and straight pores are almost nonexistent, we set the relative roughness from 0 to 0.005 and tortuosity from 1 to 2, which may have caused some deviations. The deviations arising from the uncertainties of relative roughness and tortuosity are represented by error lines in Fig. 7(b).

### 3.3. Validation with numerical method

Owing to the lack of suitable results for transient flow combined with nanoconfinement effects, we used the numerical method to solve the N–S equation and combined it with nanoconfinement effects to validate our model. The continuity equation, momentum equation, and slip velocity boundary conditions are as follows:

$$\nabla \cdot \boldsymbol{u} = 0, \tag{33}$$

$$\frac{d\boldsymbol{u}}{dt} = \boldsymbol{f} - \frac{1}{\rho_{shift}}\nabla \boldsymbol{p} + \frac{1}{\rho_{shift}}\nabla \cdot \left[\mu_{app}\boldsymbol{A}\right], \tag{34}$$

$$\boldsymbol{u}_s = l_s\left(\frac{\partial \boldsymbol{u}}{\partial r}\right)_{wall}, \tag{35}$$

where $\boldsymbol{A}$ is the first-order Rivlin–Ericksen tensor, which represents the strain rate; $\boldsymbol{u}$ is the fluid velocity vector; $\boldsymbol{f}$ is the volume force acting on the fluid; and $\boldsymbol{u}_s$ is the slip velocity.

We solved Eqs. (33)–(35) by the Galliukin finite element

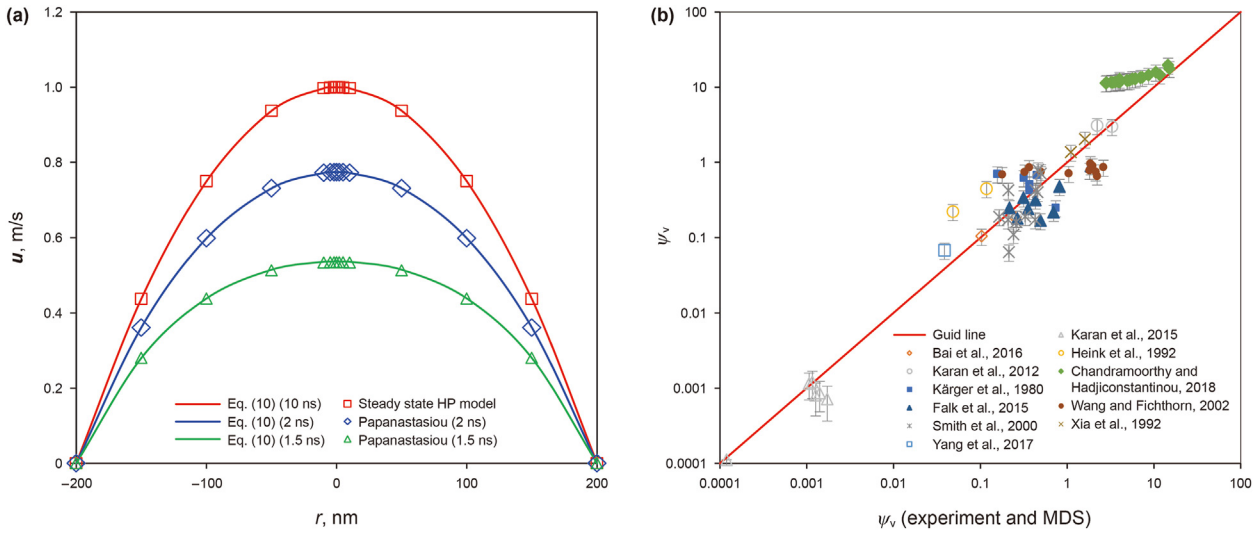


**Fig. 7.** Model validation. (**a**) Validation with the Papanastasiou model and the steady-state HP model; (**b**) Validation with experimental and molecular simulation results.

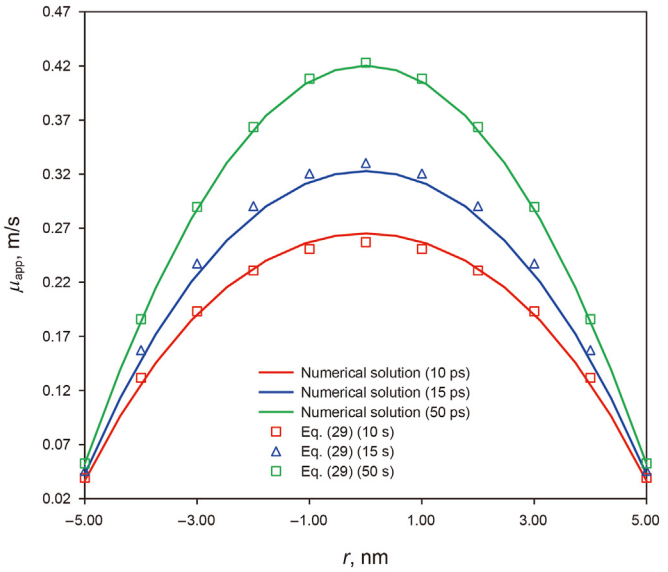


**Fig. 8.** Validation of our model proposed in Eq. (29) with the numerical simulation results.

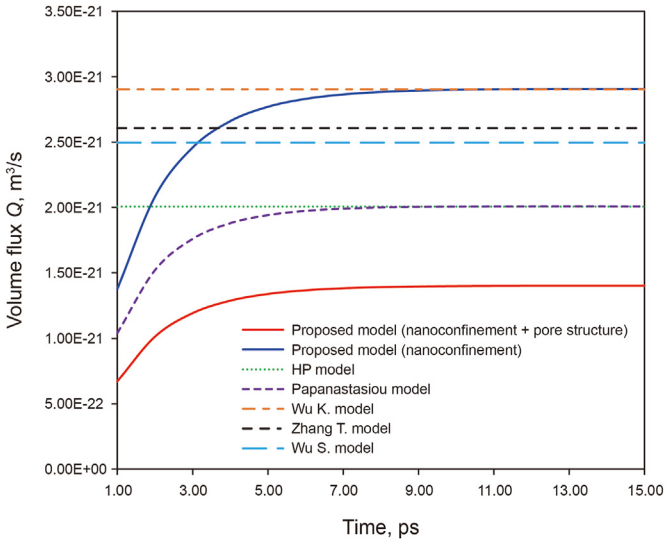


**Fig. 9.** Comparison of volume flux with other models. The pore radius ($R$) is 2 nm, and the pressure gradient ($\Delta P/L$) is $1 \times 10^{11}$ Pa/m, the liquid is hexane ($C_6H_{14}$), $\mu_b$ is $3.13 \times 10^{-4}$ Pa s, and $\rho_b$ is 660.34 kg/m$^3$.

method. The length and radius of the nanopore were set to 50 nm and 5 nm, respectively, and the computational domain was divided into 312 elements using a four-sided element. The pressure and velocity element interpolation functions were a four-node quadrilateral element and a nine-node quadrilateral element, respectively. The number of velocity nodes and pressure nodes was 1343 and 360, respectively. The density and viscosity of bulk $C_6H_{14}$ were 660 kg/m$^3$ and $3.13 \times 10^{-4}$ Pa s, respectively, and $\sigma_s^d$ was 0.02 N/m. The critical drift density, apparent viscosity, and slip length of $C_6H_{14}$ were 644 kg/m$^3$, $3.38 \times 10^{-4}$ Pa s, and 0.35 nm, respectively. As can be seen from Fig. 8, the numerical results align with those of Eq. (29) at time points 10, 15, and 50 ps, indicating the validity of our model.

### 3.4. Comparison of volume flux with other models

For the general HP model, it is known to model the macroscopic flow better. However, when the liquid is confined in the nanopores, the result of the general HP model will be biased. This will occur, for example, when the volume flux calculated by the HP model is $2.0 \times 10^{-21}$ m$^3$/s, which is lower than that of Wu K., Zhang, and Wu S. model (Wu K. et al., 2019; Zhang et al., 2019b; Wu S. et al., 2021). The effect is caused by not considering the nanoconfinement effect. For the Papanstasiou transient model, compared with the HP equation, its application is wider, and it can describe both the unsteady and steady flows. For example, in Fig. 9, when the time is less than 9 ps, it is unsteady flow; when the time is greater than 9 ps, the flow becomes steady, and the results are the same as those of the HP model. However, this model is limited to model transient flow under macroscopic conditions. Wu K. model is based on the HP model by introducing the nanoconfinement effect (homogenized effective viscosity and slip length) into the HP model. Zhang model deals with the nanoconfinement effect by dividing the liquid into two phases according to the difference in viscosity: the liquid in the pore wall region and in the pore center. Wu S. model considers the nonhomogeneous distribution of viscosity in the nanopore without homogenization and phase separation. Since it considers the oscillatory nonhomogeneous distribution of viscosity, its results are slightly lower than those of Wu K. and Zhang models. All three models are only applicable to modeling the steady flow of confined liquids; they do not incorporate the effect of pore structure characteristics. In contrast, our model has a broader scope of application, including transient flow, nanoconfinement effects, and pore structure characteristics. If the transient flow and pore structure factors are removed from our model, the model will degenerate to Wu K. model. For example, when the time is greater than 11 ps, our model generates the same results as Wu K. model. In addition, when the above three factors are considered simultaneously, the results of our model are significantly lower owing to the effect of the pore structure characteristics (roughness and tortuosity).

By comparing the above models, we can identify the main advantages of the proposed model as follows. First, we established the analytical model of transient flow through the time-dependent HP equation combined with the slip boundary conditions, which introduces the time item, density, and slip length into the HP equation. In addition, our model can reveal the effect of alkane properties on the unsteady flow characteristics under confinement conditions. Second, we established a quantitative characterization of the critical drift density, which is jointly influenced by wettability and pore size dimension, and we introduced the effect of the confined liquid density on the unsteady flow at the nanoscale. Existing studies of the phase behavior of nanoconfinement effects stopped at the drift of the critical temperature and did not extend their effects to the density and flow of liquid. Third, we integrated the transient flow with the nanoconfinement effect and pore structure characteristics to establish a more comprehensive analytical model. These three factors are important to influence the nanoscale flow behavior, especially in the flow of shale oil. In this scenario, the above three factors coexist, so neglecting any of them will yield incomplete nanoscale flow behavior. Most existing models are limited to one-sided work, such as the effect of the nanoconfinement effect on steady flow behavior, and the effect of pore structure characteristics on the liquid flow (Wu K. et al., 2019; Zhang et al., 2019b; Wu S. et al., 2021), making it hard to capture the real flow characteristics of oil in nanopores.

## 4. Results

The composition of shale is complex, including kerogen, quartz, and clay minerals. Kerogen is organic matter, whereas quartz and

**Table 1**
Pore structure data.

| Parameter | Organic matter | Inorganic matter |
|---|---|---|
| Maximum pore radius $R_{max}$, nm (Josh et al., 2012) | 44.4 | 8150.0 |
| Minimum pore radius $R_{min}$, nm (Josh et al., 2012) | 1.92 | 11.5 |
| Porosity $\phi_p$ (dimensionless) (Josh et al., 2012) | 0.03 | 0.06 |
| Average pore radius $R_{ave}$, nm | 6.43 | 30.88 |
| Pore length $L_s$, m | $5 \times 10^{-5}$ | $5 \times 10^{-5}$ |
| Average tortuosity $\tau_{ave}$ (Yu and Li, 2004) | 17.04 | 8.71 |
| Tortuous fractal dimension $D_t$ | 0.72 | 0.81 |
| $\varphi$ (dimensionless) (Fan et al., 2020) | 0.001 | 0.002 |
| $\beta$ (dimensionless) (Fan et al., 2020) | 0.02 | 0.02 |
| $(h_{max})_{R_{pmin}}/R_{pmin}$ (Yang et al., 2015(b)) | 0.05 | 0.50 |
| Wall energy $\sigma_s^d$, N/m | 0.0405 | 0.023 |

*Notes*: The average pore radius ($R_{ave}$) in Table 1 was calculated by the maximum pore radius ($R_{max}$) and minimum pore radius ($R_{min}$) and porosity ($\phi_p$) of porous media shale using the method in the literature (Yu, 2005). The average tortuosity ($\tau_{ave}$) was calculated using the method in the literature (Yu and Li, 2004).

**Table 2**
Alkane properties.

| Parameter | $C_6$ | $C_8$ | $C_{10}$ | $C_{12}$ |
|---|---|---|---|---|
| Temperature $T$, K | 293.15 | 293.15 | 293.15 | 293.15 |
| Pressure difference $\Delta p$, MPa | 5.00 | 5.00 | 5.00 | 5.00 |
| LJ size parameter $\sigma$, nm (Feng et al., 2020) | 0.63 | 0.69 | 0.73 | 0.79 |
| Critical density $\rho_c$, kg/m$^3$ | 233.06 | 232.00 | 233.00 | 227.00 |
| Fitting partner $a$ (Chouaieb et al., 2004) | 0.80 | 0.82 | 0.82 | 0.83 |
| Fitting partner $b$ (Chouaieb et al., 2004) | 0.31 | 0.29 | 0.28 | 0.27 |
| Bulk alkane critical temperature $T_{cb}$, K | 507.82 | 568.67 | 617.70 | 658.00 |
| Bulk alkane density $\rho_b$, kg/m$^3$ | 659.77 | 706.18 | 735.15 | 743.97 |
| Bulk alkane viscosity $\mu_b$, mPa s | 0.31 | 0.54 | 0.91 | 1.49 |
| Alkane surface free energy $\sigma_l$, N/m | 0.0184 | 0.0216 | 0.0238 | 0.0253 |
| Reduced relaxation time in inorganic pores $\tau_i/\tau_b$ | 1.60 | 1.63 | 1.65 | 1.68 |
| Reduced relaxation time in organic pores $\tau_i/\tau_b$ | 3.11 | 4.06 | 5.63 | 7.94 |

*Notes*: The main chemical composition of organic pores is carbon, which has a $\sigma_s^d$ of 0.00405 N/m (Zebda et al., 2008). In the system of pores with the $\sigma_s^d$ of 0.00405 N/m and $C_6H_{14}$, the reduced relaxation time is 3.11 (Fig. 3). In inorganic pores, quartz is more predominant, and its main composition is silicon, which has a $\sigma_s^d$ of 0.023 N/m (Wu et al., 2019). The reduced relaxation time in the system consisting of pores with $\sigma_s^d$ of 0.023 N/m and $C_6H_{14}$ is 1.6 (Fig. 3). Therefore, the reduced relaxation time of alkanes in organic and inorganic pores in Table 2 corresponds to the $\sigma_s^d$ of 0.0405 and 0.023 N/m, respectively.

clay minerals are inorganic matter (Cao et al., 2016, 2017; Li et al., 2021). Organic and inorganic matter differ in pore size ($R$), pore structure ($\tau$ and $\varepsilon$), and wall energy ($\sigma_s^d$). Therefore, we modeled the transport behavior of liquids (including hexane ($C_6$), octane ($C_8$), decane ($C_{10}$), and dodecane ($C_{12}$)) in organic and inorganic pores. The data used for the calculations are presented in Tables 1 and 2.

The reduced relaxation time is a key parameter in practical applications, and the following explanation is given for the acquisition of this parameter: The reduced relaxation time of alkanes in nanopores depends strongly on the wall energy ($\sigma_s^d$) and alkane surface tension (alkane surface free energy). As $\sigma_s^d$ increases, the relaxation time also increases. This is because the increase in $\sigma_s^d$ leads to the densification of the liquid molecules in the wall region, resulting in a decrease in the disorder and mobility of the molecules. In addition, the shape, chain length, and intermolecular interactions of the alkane molecules have a significant effect on the relaxation time. For example, the longer the alkane carbon chain, the longer the relaxation time. Moreover, the mineral fraction of nanopores and the alkane type are known, and a reduced relaxation time can be obtained by molecular simulations or experiments, including Rayleigh-wing scattering and Raman spectroscopy. Wu et al. (2019) obtained the relationship between $\sigma_s^d$ and the reduced relaxation time by molecular simulation methods (Fig. 3). Furthermore, the interaction between organic matter and alkanes is stronger compared to inorganic matter (Zhang et al., 2017), which also results in larger alkane relaxation times in organic matter pores than inorganic pores. Note that the composition of organic and inorganic pores has other components in addition to carbon and quartz, and the mineral components in different areas are different. This causes the difference between $\sigma_s^d$ and the reduced relaxation time. Therefore, in practical use, $\sigma_s^d$ should be determined by experimentation, and then the reduced relaxation time of the corresponding alkane should be obtained as in Fig. 3. In addition, if the flow of multi-component alkanes is to be simulated, a multi-component setting is performed in the molecular simulation to obtain the reduced relaxation time.

The results are shown in Fig. 10. The volumetric flow rate enhancement ($\psi_v$) is less than 0.1 for organic matter and more than 0.1 for inorganic matter because of the greater tortuosity and stronger wall–liquid interaction in organic pores than in inorganic pores. In addition, the higher the carbon number, the higher the flow development rate. As the carbon number increases, the liquid–liquid interaction increases more than the wall–liquid interaction, leading to a more significant slip.

Furthermore, the transport of different alkanes in organic and inorganic pores shows different characteristics. For organic pores, in Fig. 10(a), the $\psi_v$ of $C_{12}$ increases with time, whereas that of $C_6$–$C_{10}$ decreases. For $C_{12}$ confined in nanopores, the nanoconfinement effect, such as slip, critical drift density, and apparent viscosity, makes the flow development rate greater than that of bulk $C_{12}$. Thus, $\psi_v$ increases with time. For $C_6$–$C_{10}$ confined in nanopores, the combined effect makes the flow development rate smaller than that of bulk $C_6$–$C_{10}$, so $\psi_v$ decreases with time. For inorganic pores, as Fig. 10(b) shows, the $\psi_v$ of $C_6$–$C_{12}$ alkanes increases with time, indicating that the nanoconfinement effect makes a positive contribution to the flow development rates. In

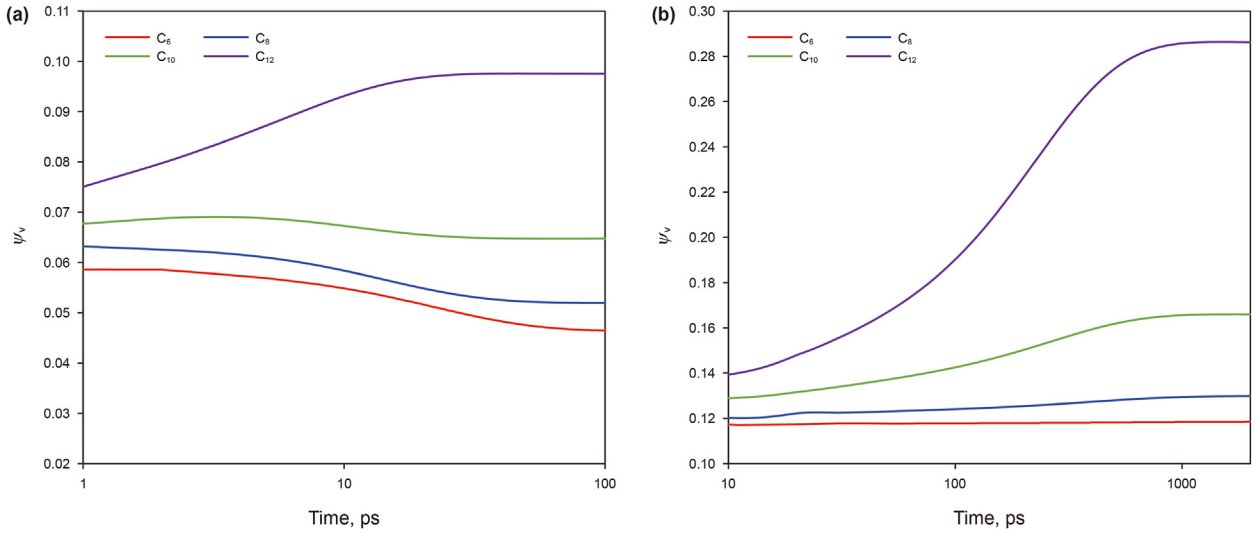


**Fig. 10.** Transport of different alkanes in nanopore of shale in organic pores (**a**) and inorganic pores (**b**).

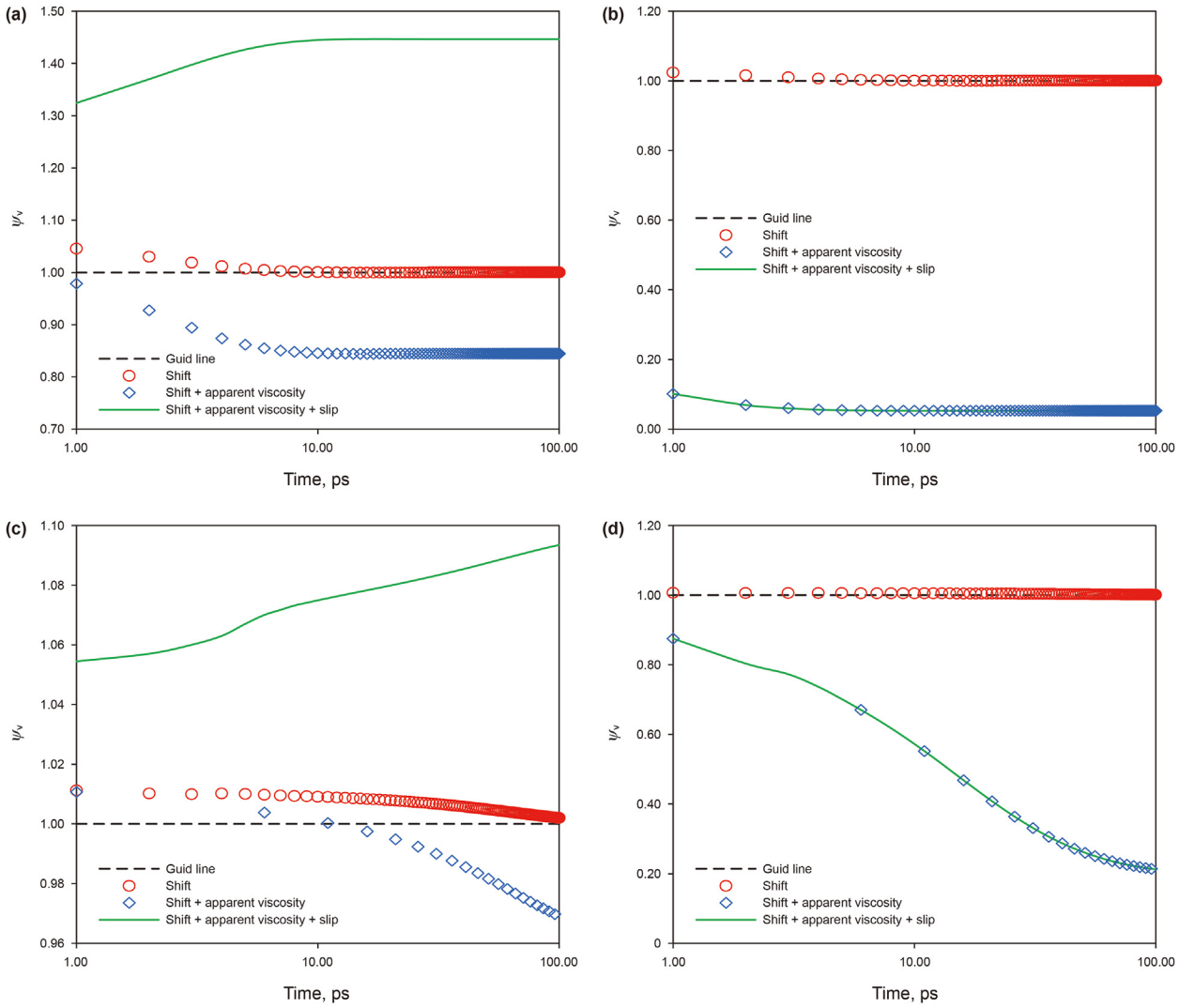


**Fig. 11.** The effect of nanoconfinement effect on the flow behavior of $C_6$. (**a**) $R$ is 2 nm, and $\sigma_s^d$ is 0.02 N/m; (**b**) $R$ is 2 nm, and $\sigma_s^d$ is 0.16 N/m; (**c**) $R$ is 10 nm, and $\sigma_s^d$ is 0.02/m; (**d**) $R$ is 10 nm, and $\sigma_s^d$ is 0.16 N/m.

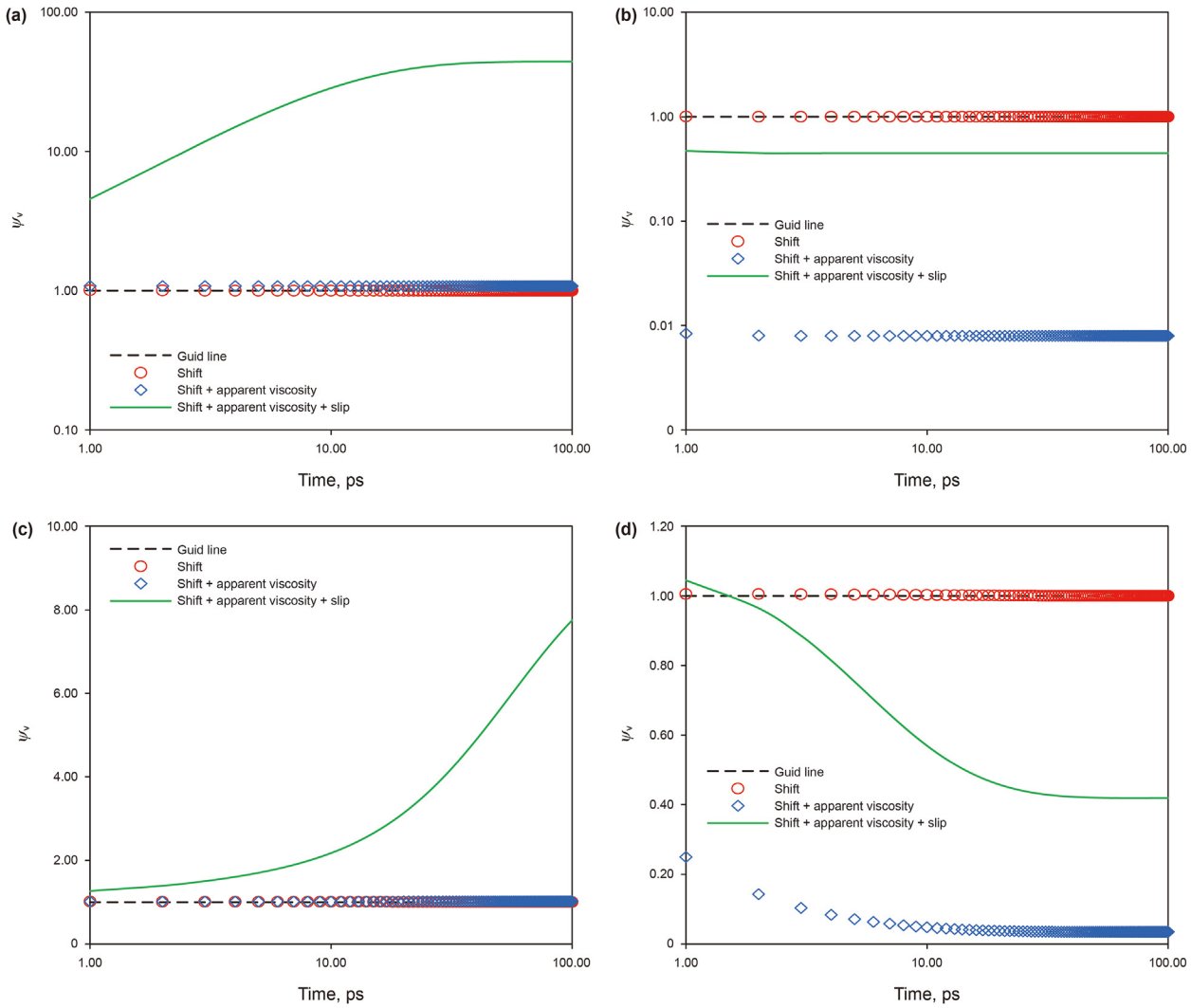


**Fig. 12.** The effect of nanoconfinement effect on the flow characteristics of $C_{12}$: (**a**) $R$ is 2 nm and $\sigma_s^d$ is 0.02 N/m; (**b**) $R$ is 2 nm and $\sigma_s^d$ is 0.16 N/m; (**c**) $R$ is 10 nm and $\sigma_s^d$ is 0.02 N/m; (**d**) $R$ is 10 nm, and $\sigma_s^d$ is 0.16 N/m.

inorganic pores, the wall energy of the pore is smaller, so the positive effect of critical drift density and slip is larger, and the negative inhibition of the apparent viscosity is smaller.

## 5. Discussion

### 5.1. Unsteady flow behavior

#### 5.1.1. Effect of nanoconfinement effects on the unsteady flow

We analyzed the unsteady transport characteristics of hexane and dodecane under different $R$ and $\sigma_s^d$, respectively. As Figs. 11 and 12 show, the critical drift density causes a slight increase in the flow development rate, which occurs mainly in the initial stage. However, this effect gradually disappears with time. The density affects only the volume flow development rate in the unsteady state. In addition, the effect of critical drift density on the flow development rate is most pronounced at smaller pore radii, lower wall energies, and shorter chain lengths. The equilibrium diffusion pressure makes the interaction of the low-energy wall alkane stronger than that of the high-energy wall alkane.

In addition, when we further considered the apparent viscosity, the ratios of the apparent viscosity of confined alkanes to the bulk alkane viscosity for $C_6$ with the low-energy wall at 2 nm, the high-energy wall at 2 nm, the low-energy wall at 10 nm, and the high-energy wall at 10 nm are 1.18, 2.88, 1.04, and 1.41, respectively. These results indicate that the apparent viscosity inhibits the flow development rate and can offset the positive contribution of the critical drift density, resulting in a decrease in the volumetric flow enhancement rate with time (Fig. 11). In addition, the apparent viscosity of $C_6$ in the high-energy wall pores is larger than that in the low-energy wall pores. Therefore, the former stabilizes earlier. Furthermore, the apparent viscosity of $C_6$ in pores with a radius of 10 nm is less than that of pores with a radius of 2 nm. Thus, the former takes longer to stabilize. When further considering slip, the slip of $C_6$ in the pores of the low-energy wall with a radius of 2 nm, the high-energy wall with a radius of 2 nm, the low-energy wall with a radius of 10 nm, and the high-energy wall with a radius 10 nm are 0.356, 0, 0.356, and 0 nm, respectively. The results indicate that the pores of the higher-energy wall do not have a slip effect (Fig. 11(b)–(d)). Moreover, in the pores of the low-energy walls, the volume flow enhancement rate increases with time under the combined effect of critical drift density, apparent viscosity, and slip, so the promotion effect of the critical drift density and slip on the flow development rate is larger than the inhibitory effect of

viscosity (Fig. 11(a)–(c)).

For $C_{12}$, the ratios of the apparent viscosity of confined alkanes to the viscosity of bulk alkanes in pores with low-energy walls of 2 nm, high-energy walls of 2 nm, low-energy walls of 10 nm, and high-energy walls of 10 nm are 0.92, 6.27, 0.98, and 2.17, respectively. When we consider the dual effect of critical drift density and apparent viscosity, the volumetric flow enhancement rate decreases with time only in the high-energy pores with a radius of 10 nm. The variation of the volumetric flow enhancement rate with time is small, however, in the other three cases. For the low-energy pores with radii of 2 and 10 nm, the apparent viscosity of confined alkanes is slightly lower than that of bulk alkane. Thus, the difference in their flow development rates is small, which is why the change in the volumetric flow enhancement rate with time is small. In high-energy pores with a radius of 2 nm, the apparent viscosity of the confined alkanes is much larger than that of the bulk alkanes. Hence, the flow stabilizes early. When considering slip further, the slip in the pores with low-energy walls of 2 nm, high-energy walls of 2 nm, low-energy walls of 10 nm, and high-energy walls of 10 nm is 11, 3.8, 11, and 3.8 nm, respectively. As Fig. 12(a)–(c) shows, the volumetric flow enhancement rate increases with time in the low-energy pores. This is because the slip, apparent viscosity, and critical drift density all contribute to the flow development rate. By contrast, in the high-energy pores, the positive promotion effect of the slip and critical drift density on the flow development rate is offset by the negative inhibition effect of the apparent viscosity, as in Fig. 12(b) and (d). Thus, the volumetric flow enhancement rate does not increase with time.

### 5.1.2. Effect of pore structure on unsteady flow

We further analyzed the effect of pore structure on the volumetric flow enhancement rate based on the effect of the nanoconfinement effect, as Figs. 13 and 14 show. For $C_6$ alkanes, when $\sigma_s^d$ is low, the volumetric flow enhancement rate is slightly reduced if the roughness is considered, but it remains at around 1. This result indicates that the positive contribution of the nanoconfinement effect is offset by the negative effect of roughness. Additionally, the flow capacity of the confined alkanes for this case is comparable to that of the bulk alkanes, as shown in Fig. 13(a)–(c). When $\sigma_s^d$ is higher, both the nanoconfinement effect and the roughness have a negative inhibitory role. The volume flow enhancement rate is less than 1, indicating that the flow capacity of the confined $C_6$ is less

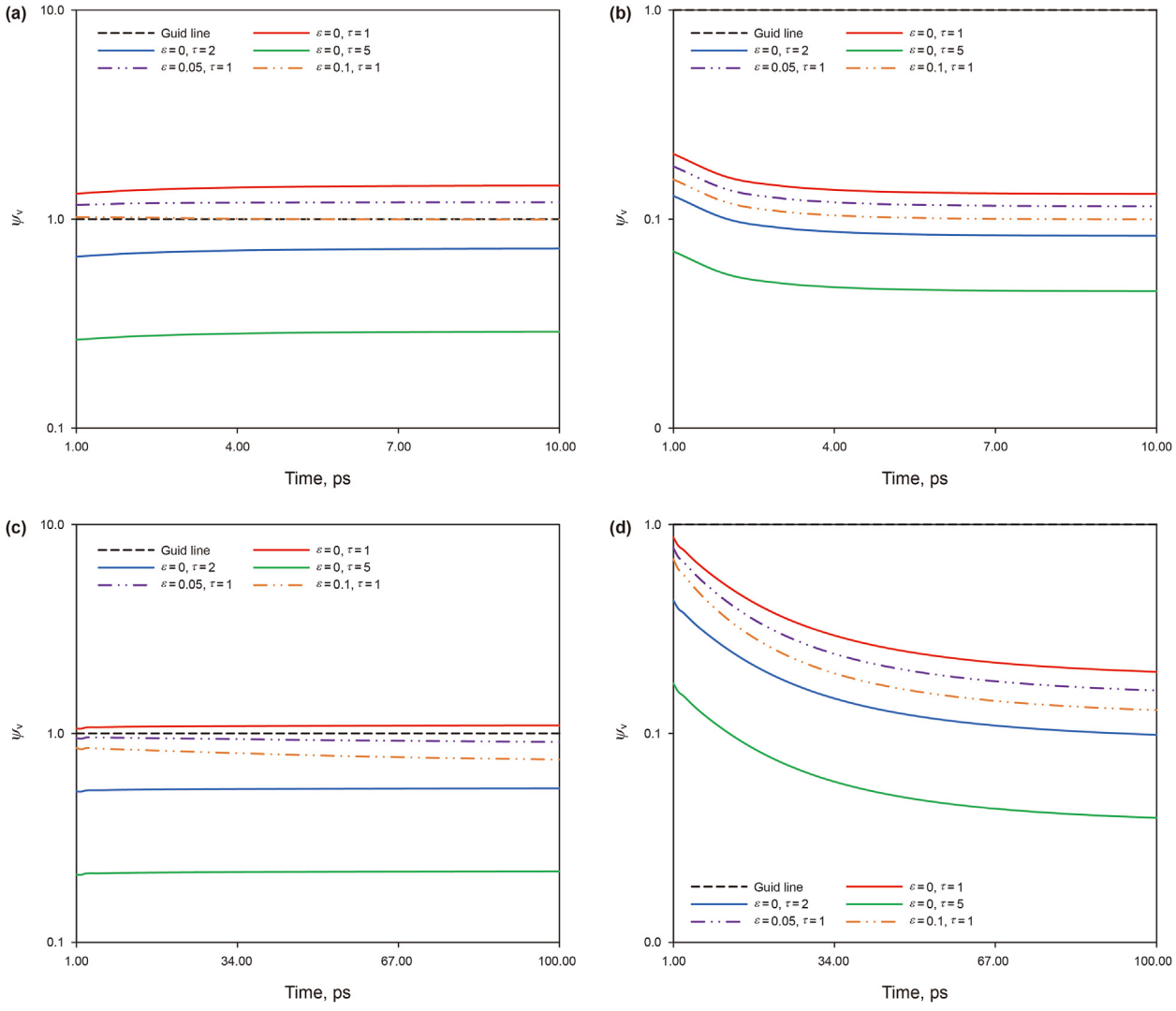


**Fig. 13.** Effect of pore structure on the flow characteristics of $C_6$. (**a**) $R$ is 2 nm, and $\sigma_s^d$ is 0.05 N/m; (**b**) $R$ is 2 nm, and $\sigma_s^d$ is 0.16 N/m; (**c**) $R$ is 10 nm, and $\sigma_s^d$ is 0.05 N/m; (**d**) $R$ is 10 nm, and $\sigma_s^d$ is 0.16 N/m.

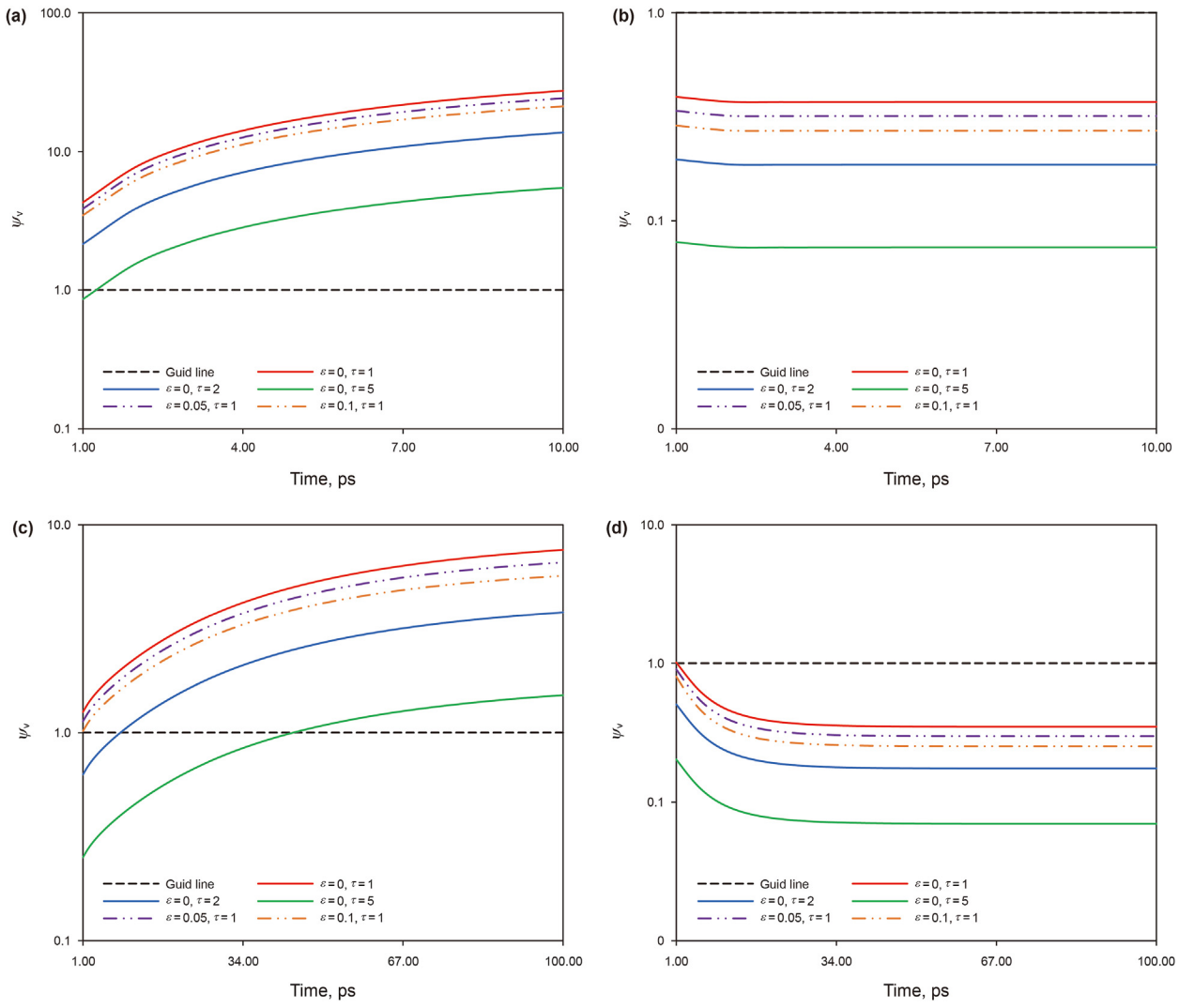


**Fig. 14.** Effect of pore structure on the flow behavior of $C_6$. (**a**) $R$ is 2 nm, and $\sigma_s^d$ is 0.05 N/m; (**b**) $R$ is 2 nm, and $\sigma_s^d$ is 0.16 N/m; (**c**) $R$ is 10 nm, and $\sigma_s^d$ is 0.05 N/m; (**d**) $R$ is 10 nm, and $\sigma_s^d$ is 0.16 N/m.

than that of the bulk $C_6$. When tortuosity is further considered, the volume flow enhancement rate is less than 1, regardless of the high or low $\sigma_s^d$.

For $C_{12}$ alkanes, in the low-energy wall pores with a radius of 2 nm, the volumetric flow enhancement rate is still greater than 1 despite the consideration of roughness and tortuosity, indicating that the positive promotion effect caused by the nanoconfinement effect is greater than the negative inhibition effect caused by roughness and tortuosity (Fig. 14(a)). In high-energy wall pores with a radius of 2 nm (Fig. 14(b)), however, the nanoconfinement effect is inhibitory to the flow capacity. In addition, the volume flow enhancement rate is further reduced after considering the effects of roughness and tortuosity. As the pore radius increases, the effect of the nanoconfinement effect weakens. For pores of low-energy wall with a radius of 10 nm (Fig. 14(c)), the volumetric flow enhancement rate is greater than 1 if roughness and tortuosity are not considered. However, for the two cases with a tortuosity of 2 and 5, the volumetric flow enhancement rate is less than 1 at the initial stage and gradually becomes greater than 1 with time. For high-energy wall pores with a radius of 10 nm (Fig. 14(d)), the nanoconfinement effect, roughness, and tortuosity all play a negative role, and the volumetric flow enhancement rates are less than 1.

### 5.2. Steady flow behavior

We analyzed the steady transport behavior using the results of Eq. (32) as time tended to infinity. To illustrate the effect of the critical drift density on the steady flow behavior, we defined the mass flow enhancement rate ($\psi_m$) (volumetric flow enhancement rate multiplied by the critical drift density) to describe the steady transport behavior. As Fig. 15(a) shows, $\psi_m$ can span six orders of magnitude in the range of a pore radius of 1.5 nm and $\sigma_s^d$ of 0.02–0.2 N/m. In addition, $\psi_m$ gradually decreases with an increasing $\sigma_s^d$ and decreasing carbon number. Furthermore, the critical drift density has a relatively large negative effect on $\psi_m$ when $\sigma_s^d$ is small and the alkane carbon number of alkanes is low, and its effect gradually decreases as $\sigma_s^d$ increases and the alkane carbon number increases (Fig. 15(c)). Moreover, Fig. 15(b) shows that $\psi_m$ tends to 1 as the pore diameter increases, regardless of whether it is higher or lower than the carbon number. As Fig. 15(d) shows, for a pore of a small radius, the critical drift density has the greatest effect.

As Fig. 16 shows, $\psi_m$ decreases as the tortuosity increases. For $C_{10}$ and $C_{12}$, $\psi_m$ is still greater than 1 or slightly less than 1 at an $\sigma_s^d$ of 0.02 N/m and an $R$ of 1.5 nm. This indicates that the positive effect of

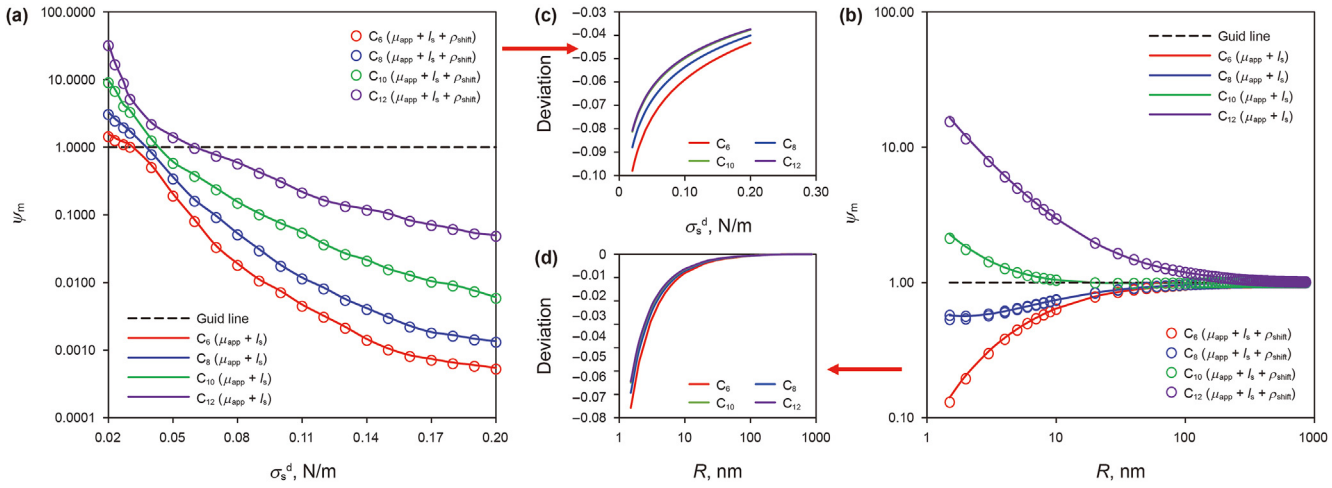


**Fig. 15.** Effect of the nanoconfinement effect on steady flow with $R$ of 1.5 nm, $T$ of 293.15, $\varepsilon$ of 0, and $\tau$ of 1. (**a**) Effect of $\sigma_s^d$ on the mass flow enhancement rate; (**b**) Effect of pore radius on the mass flow enhancement rate; (**c**) Deviation due to neglecting $\rho_{shift}$ (variation with $\sigma_s^d$); (**d**) Deviation due to neglecting $\rho_{shift}$ (variation with pore radius).

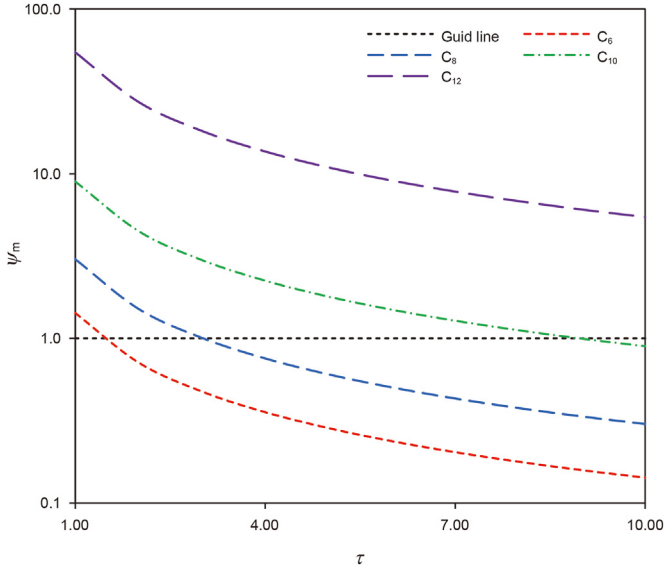


**Fig. 16.** Effect of tortuosity on mass flow enhancement rate with $\sigma_s^d$ of 0.02 N/m, $R$ of 1.5 nm, $\varepsilon$ of 0, and $T$ of 293.15 K.

nanoconfinement can offset the negative effect of tortuosity. For $C_6$ and $C_{10}$, the positive effect of nanoconfinement is weaker, so $\psi_m$ gradually becomes lower than 1 with an increase in tortuosity.

As Fig. 17(a) shows, $\psi_m$ gradually decreases as $\beta$ increases. This is because the larger the value of $\beta$, the larger the volume of the roughness element and the greater the flow resistance, leading to a decrease in $\psi_m$. As Fig. 17(b) shows, $\psi_m$ gradually decreases as $\gamma$ increases. The larger the value of $\gamma$, the larger the maximum height of the roughness element and the more the flow resistance is enhanced, causing $\psi_m$ to decrease. As Fig. 17(c) shows, $\psi_m$ gradually decreases with an increase in $\varphi$. The larger $\varphi$ indicates more roughness elements per unit area, leading to an increase in flow resistance. Therefore, $\psi_m$ decreases. Notably, as Fig. 17(c) shows, the larger the value of $D_c$, the larger the value of $\psi_m$. This is because under the condition that $\varphi$ is fixed, the larger the value of $D_c$, the smaller the value of $\beta$. Thus, the volume of the roughness element is smaller, leading to a weakening of the flow resistance.

## 6. Conclusions

In this study, we combined the critical drift density, apparent viscosity, and slip length (characterizing the nanoconfinement effect), as well as the tortuosity and roughness (characterizing the pore structure features), with transient Poiseuille flow to obtain a transient flow model of oil in shale nanopores. The model can reveal the effect of the nanoconfinement effect and the pore structure characteristics on oil transport in unsteady and steady states in shale nanopores. The following conclusions can be drawn.

(1) Different alkanes have different transport characteristics in organic and inorganic pores. In organic matter pores, the volume flow enhancement rates of $C_6$–$C_{12}$ alkanes were all less than 0.1. It increased with time only for $C_{12}$ alkanes, whereas it decreased with time for $C_6$–$C_{10}$ alkanes. In the inorganic pores, the volume flux enhancement rates for $C_6$–$C_{12}$ alkanes were all greater than 0.1 and increased with time.

(2) The critical drift density makes a positive contribution to the volume flow development rate in the unsteady state and a negative inhibitory effect on the mass flow rate in the steady state. Its effect is clearest when the pore radius was small, the wall energy was low, and the alkane chain length was short. In the unsteady state stage, when the pore radius was 2 nm, the dispersion force component of wall energy was 0.02 N/m, and the fluid was $C_6H_{12}$, the effect of the critical drift density on the volumetric flow rate enhancement was 4.5%. Under the same conditions as above, the effect on the mass flow rate enhancement could rise to −10% in the steady state stage.

(3) The variation characteristics of the volumetric flow enhancement rate in the unsteady state are complex, either greater than 1 or less than 1, depending on the combined effect of nanoconfinement and pore structure characteristics. The volumetric flow enhancement rate may have increased or decreased with time, depending mainly on the nanoconfinement. If the nanoconfinement made the volume flow development rate of the confined alkane greater than that of the bulk alkane, the volumetric flow enhancement rate increased with time, and vice versa.

(4) Nanoconfinement has a great influence on the mass flow enhancement rate. It could span six orders of magnitude in

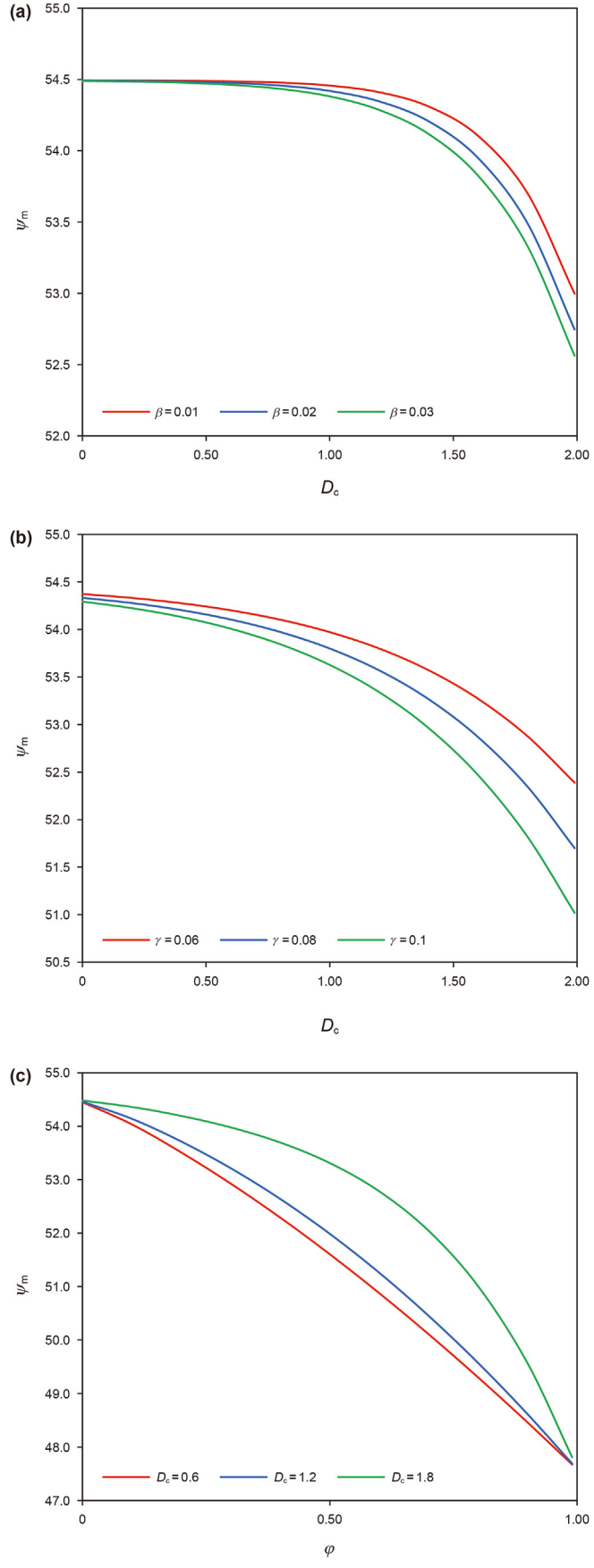


**Fig. 17.** Effect of roughness fractal parameters on the mass flow enhancement rate: $\sigma_s^d$ is 0.02 N/m, $R$ is 1.5 nm, $T$ is 293.15 K, and tortuosity is 1. (**a**) Variation of $\psi_m$ with $D_c$ under different $\beta$, $\gamma = (h_{max})_{R_{pmin}}/R_{pmin} = 0.1$; (**b**) Variation of $\psi_m$ with $D_c$ under different $\gamma$, $\beta = 0.02$; (**c**) Variation of $\psi_m$ with $\varphi$ under different $D_c$, $\gamma = 0.1$.

the range of a pore radius of 1.5 nm and wall energy of 0.02–0.2 N/m. It reached a maximum of 31.8 and a minimum of $5.23 \times 10^{-4}$. The tortuosity and surface roughness also have a significant effect on the mass flow enhancement rate. When the tortuosity was 10, the mass flow enhancement rate could be reduced by 90% relative to a straight pore. When the surface roughness was 0.03, the mass flow enhancement rate could be reduced by 12% relative to smooth pores.

## Declaration of competing interest

The authors declare that they have no known competing financial interests or personal relationships that could have appeared to influence the work reported in this paper.

## Acknowledgments

This work was supported by the National Natural Science Foundation for Youths of China (Grant No. 12201374), the Scientific Research Foundation of Education Department of Shaanxi Province (Grant No. 22JK0315), the Research Foundation for the Doctoral Program of Shaanxi University of Technology (Grant No. SLGRCQD2136), the Key R&D Plan, Shaanxi Province (2022GY-138), and the Science and Technology Plan Project, Guizhou Province ([2022]ZD005).

## Appendix A. Supplementary data

Supplementary data to this article can be found online at https://doi.org/10.1016/j.petsci.2023.07.015.

## References

Argyris, D., Ashby, P.D., Striolo, A., 2011. Structure and orientation of interfacial water determine atomic force microscopy results: insights from molecular dynamics simulations. ACS Nano 5 (3), 2215–2223. https://doi.org/10.1021/nn103454m.

Blake, T.D., 1990. Slip between a liquid and a solid: D.M. Tolstoi's (1952) theory reconsidered. Colloid. Surface. 47, 135–145. https://doi.org/10.1016/0166-6622(90)80068-F.

Cao, B.Y., Chen, M., Guo, Z.Y., 2006. Liquid flow in surface-nanostructured channels studied by molecular dynamics simulation. Phys. Rev. E 74 (6), 6311. https://doi.org/10.1103/PhysRevE.74.066311.

Cao, C., Li, T., Shi, J., Zhang, L., Fu, S., Wang, B., Wang, H., 2016. A new approach for measuring the permeability of shale featuring adsorption and ultra-low permeability. J. Nat. Gas Sci. Eng. 30, 1875–5100. https://doi.org/10.1016/j.petrol.2021.109191.

Cao, C., Zhao, Q., Gao, C., Sun, J., Xu, J., Zhang, P., Zhang, L., 2017. Discrete fracture model with multi-field coupling transport for shale gas reservoirs. J. Petrol. Sci. Eng. 158, 107–119. https://doi.org/10.1016/j.petrol.2017.08.033.

Chen, L., Kang, Q., Dai, Z., Viswanathan, H.S., Tao, W., 2015. Permeability prediction of shale matrix reconstructed using the elementary building block model. Fuel 160, 346–356. https://doi.org/10.1016/j.fuel.2015.07.070.

Chouaieb, O., Ghazouani, J., Bellagi, A., 2004. Simple correlations for saturated liquid and vapor densities of pure fluids. Thermochim. Acta 424 (1), 43–51. https://doi.org/10.1016/j.tca.2004.05.017.

Cui, J., 2019. Oil transport in shale nanopores and micro-fractures: modeling and analysis. J. Petrol. Sci. Eng. 178, 640–648. https://doi.org/10.1016/j.petrol.2019.03.088.

Fan, D., Ettehadtavakkol, A., Wang, W., 2020. Apparent liquid permeability in mixed-wet shale permeable media. Transport Porous Media 134 (3), 651–677. https://doi.org/10.1007/s11242-020-01462-5.

Farrer, R.A., Fourkas, J.T., 2003. Orientational dynamics of liquids confined in nanoporous sol–gel glasses studied by optical kerr effect spectroscopy. Acc. Chem. Res. 36 (8), 605–612. https://doi.org/10.1021/ar0200302.

Feng, D., Wu, K., Bakhshian, S., Hosseini, S.A., Li, J., Li, X., 2020. Nanoconfinement effect on surface tension: perspectives from molecular potential theory. Langmuir 36 (30), 8764–8776. https://doi.org/10.1021/acs.langmuir.0c01050.

Feng, D., Bakhshian, S., Wu, K., Song, Z., Ren, B., Li, J., Hosseini, S.A., Li, X., 2021. Wettability effects on phase behavior and interfacial tension in shale nanopores. Fuel 290, 119983. https://doi.org/10.1016/j.fuel.2020.119983.

Feng, Q., Xu, S., Wang, S., Li, Y., Gao, F., Xu, Y., 2019. Apparent permeability model for shale oil with multiple mechanisms. J. Petrol. Sci. Eng. 175, 814–827. https://

doi.org/10.1016/j.petrol.2019.01.038.
Fowkes, F.M., 1964. Attractive forces at interfaces. Ind. Eng. Chem. 56 (12), 40–52. https://doi.org/10.1021/ie50660a008.
Fowkes, F.M., McCarthy, D.C., Mostafa, M.A., 1980. Contact angles and the equilibrium spreading pressures of liquids on hydrophobic solids. J. Colloid Interface Sci. 78 (1), 200–206. https://doi.org/10.1016/0021-9797(80)90508-1.
Holt, J.K., Park, H.G., Wang, Y., Stadermann, M., Artyukhin, A.B., Grigoropoulos, C.P., Noy, A., Bakajin, O., 2006. Fast mass transport through sub-2-nanometer carbon nanotubes. Science 312 (5776), 1034–1037. https://doi.org/10.1126/science.1126298.
Javadpour, F., Ettehadtavakkol, A., 2015. Gas transport processes in shale. Fundamentals of Gas Shale Reservoirs 245–266. https://doi.org/10.1002/9781119039228.ch11.
Jin, Y., Dong, J., Zhang, X., Li, X., Wu, Y., 2017. Scale and size effects on fluid flow through self-affine rough fractures. Int. J. Heat Mass Tran. 105, 443–451. https://doi.org/10.1016/j.ijheatmasstransfer.2016.10.010.
Josh, M., Esteban, L., Delle Piane, C., Sarout, J., Dewhurst, D.N., Clennell, M.B., 2012. Laboratory characterisation of shale properties. J. Petrol. Sci. Eng. 88–89, 107–124. https://doi.org/10.1016/j.petrol.2012.01.023.
Kobayashi, K., Liang, Y., Amano, K., Murata, S., Matsuoka, T., Takahashi, S., Nishi, N., Sakka, T., 2016. Molecular dynamics simulation of atomic force microscopy at the water-muscovite interface: hydration layer structure and force analysis. Langmuir 32 (15), 3608–3616. https://doi.org/10.1021/acs.langmuir.5b04277.
Lee, J., Babadagli, T., 2021. Effect of roughness on fluid flow and solute transport in a single fracture: a review of recent developments, current trends, and future research. J. Nat. Gas Sci. Eng. 91, 103971. https://doi.org/10.1016/j.jngse.2021.103971.
Li, J., Kong, X., Lu, D., Liu, Z., 2015. Italicized carbon nanotube facilitating water transport: a molecular dynamics simulation. Sci. Bull. 60. https://doi.org/10.1007/s11434-015-0888-7.
Li, R., Chen, Z., Wu, K., Liu, X., Dou, L., Yang, S., Xu, J., 2020. A fractal model for gas-water relative permeability curve in shale rocks. J. Nat. Gas Sci. Eng. 81, 103417. https://doi.org/10.1016/j.jngse.2020.103417.
Li, R., Chen, Z., Wu, K., Hao, H., Xu, J., 2021. An analytical model for water-oil two-phase flow in inorganic nanopores in shale oil reservoirs. Petrol. Sci. 18 (6), 12. https://doi.org/10.1016/j.petsci.2021.09.005.
Li, X., Fan, J., Yu, H., Zhu, Y., Wu, H., 2018. Lattice Boltzmann method simulations about shale gas flow in contracting nano-channels. Int. J. Heat Mass Tran. 122, 1210–1221. https://doi.org/10.1016/j.ijheatmasstransfer.2018.02.066.
Liu, Y., Zou, S., He, Y., Sun, S., Ju, Y., Meng, Q., Cai, J., 2021. Influence of fractal surface roughness on multiphase flow behavior: lattice Boltzmann simulation. Int. J. Multiphas. Flow, 103497. https://doi.org/10.1016/j.ijmultiphaseflow.2020.103497.
Ma, M.D., Shen, L., Sheridan, J., Liu, J.Z., Chen, C., Zheng, Q., 2011. Friction of water slipping in carbon nanotubes. Phys. Rev. E. 83 (3), 036316. https://doi.org/10.1103/PhysRevE.83.036316.
Majumder, M., Chopra, N., Andrews, R., Hinds, B.J., 2005. Nanoscale hydrodynamics: enhanced flow in carbon nanotubes. Nature 438 (7064), 44. https://doi.org/10.1038/43844a.
Marmur, A., 2006. Soft contact: measurement and interpretation of contact angles. Soft Matter 2 (1), 12–17. https://doi.org/10.1039/b514811c.
Mattia, D., Calabrò, F., 2012. Explaining high flow rate of water in carbon nanotubes via solid–liquid molecular interactions. Microfluid. Nanofluidics 13 (1), 125–130. https://doi.org/10.1007/s10404-012-0949-z.
Miao, T., Yang, S., Long, Z., Yu, B., 2015. Fractal analysis of permeability of dual-porosity media embedded with random fractures. Int. J. Heat Mass Tran. 88, 814–821. https://doi.org/10.1016/j.ijheatmasstransfer.2015.05.004.
Myers, T.G., 2011. Why are slip lengths so large in carbon nanotubes? Microfluid. Nanofluidics 10 (5), 1141–1145. https://doi.org/10.1007/s10404-010-0752-7.
Papanastasiou, T.C., Georgiou, G.C., Alexandrou, A.N., 1999. Viscous Fluid Flow. CRC Press.
Podolska, N.I., Zhmakin, A.I., 2013. Water flow in micro- and nanochannels. Molecular dynamics simulations. J. Phys. Conf. 461, 012034. https://doi.org/10.1088/1742-6596/461/1/012034.
Qiu, T., Meng, X.W., Huang, J.P., 2015. Nonstraight nanochannels transfer water faster than straight nanochannels. J. Phys. Chem. B 119 (4), 1496–1502. https://doi.org/10.1021/jp511262w.
Rustamov, N., Douglas, C.C., Aryana, S.A., 2023. Scalable simulation of pressure gradient-driven transport of rarefied gases in complex permeable media using lattice Boltzmann method. Fluid 8 (1), 1. https://doi.org/10.3390/fluids8010001.
Secchi, E., Marbach, S., Niguès, A., Stein, D., Siria, A., Bocquet, L., 2016. Massive radius-dependent flow slippage in carbon nanotubes. Nature 537 (7619), 210–213. https://doi.org/10.1038/nature19315.
Sendner, C., Horinek, D., Bocquet, L., Netz, R.R., 2009. Interfacial water at hydrophobic and hydrophilic surfaces: slip, viscosity, and diffusion. Langmuir 25 (18), 10768–10781. https://doi.org/10.1021/la901314b.
Shaat, M., Zheng, Y., 2019. Fluidity and phase transitions of water in hydrophobic and hydrophilic nanotubes. Sci. Rep. 9 (1). https://doi.org/10.1038/s41598-019-42101-4.
Tan, S.P., Barsotti, E., Piri, M., 2020. Criticality of confined fluids based on the tensile strength of liquids. Ind. Eng. Chem. Res. 59 (22), 10673–10688. https://doi.org/10.1021/acs.iecr.0c01848.
Tao, J., Song, X., Bao, B., Zhao, S., Liu, H., 2020. The role of surface wettability on water transport through membranes. Chem. Eng. Sci. 219, 115602. https://doi.org/10.1016/j.ces.2020.115602.
Thomas, J.A., McGaughey, A.J.H., 2008. Density, distribution, and orientation of water molecules inside and outside carbon nanotubes. J. Chem. Phys. 128 (8). https://doi.org/10.1063/1.2837297, 084715-084715.
Thomas, J.A., McGaughey, A.J.H., 2009. Water flow in carbon nanotubes: transition to subcontinuum transport. Phys. Rev. Lett. 102 (18). https://doi.org/10.1103/PhysRevLett.102.184502, 184502-184502.
Tian, Z., Wei, W., Zhou, S., Sun, C., Rezaee, R., Cai, J., 2022. Impacts of gas properties and transport mechanisms on the permeability of shale at pore and core scale. Energy 244. https://doi.org/10.1016/j.energy.2021.122707.
Wang, F., Jiao, L., Lian, P., Zeng, J., 2019c. Apparent gas permeability, intrinsic permeability and liquid permeability of fractal porous media: carbonate rock study with experiments and mathematical modelling. J. Petrol. Sci. Eng. 173, 1304–1315. https://doi.org/10.1016/j.petrol.2018.10.095.
Wang, H., Yuliang, S., Wang, W., Sheng, G., Li, H., Zafar, A., 2019a. Enhanced water flow and apparent viscosity model considering wettability and shape effects. Fuel 253, 1351–1360. https://doi.org/10.1016/j.fuel.2019.05.098.
Wang, H., Su, Y., Zhao, Z., Wang, W., Sheng, G., Zhan, S., 2019b. Apparent permeability model for shale oil transport through elliptic nanopores considering wall-oil interaction. J. Petrol. Sci. Eng. 176, 1041–1052. https://doi.org/10.1016/j.petrol.2019.02.027.
Wang, Q., Cheng, Z., 2019. A fractal model of water transport in shale reservoirs. Chem. Eng. Sci. 198, 62–73. https://doi.org/10.1016/j.ces.2018.12.042.
Wang, S., Javadpour, F., Feng, Q., 2016. Molecular dynamics simulations of oil transport through inorganic nanopores in shale. Fuel 171, 74–86. https://doi.org/10.1016/j.fuel.2015.12.071.
Wang, Y., Aryana, S.A., 2021. Coupled confined phase behavior and transport of methane in slit nanopores. Chem. Eng. J. 404, 126502. https://doi.org/10.1016/j.cej.2020.126502.
Wu, K., Chen, Z., Li, J., Lei, Z., Xu, J., Wang, K., Li, R., Dong, X., Peng, Y., Yang, S., Zhang, F., Chen, Z., Gao, Y., 2019. Nanoconfinement effect on *n*-alkane flow. J. Phys. Chem. C 123 (26), 16456–16461. https://doi.org/10.1021/acs.jpcc.9b03903.
Wu, K., Chen, Z., Li, J., Li, X., Xu, J., Dong, X., 2017. Wettability effect on nanoconfined water flow. Proc. Natl. Acad. Sci. USA 114 (13), 3358–3363. https://doi.org/10.1073/pnas.1612608114.
Wu, S., Li, Z., Zhang, C., Lv, G., Zhou, P., 2021. Nanohydrodynamic model and transport mechanisms of tight oil confined in nanopores considering liquid–solid molecular interaction effect. Ind. Eng. Chem. Res. 60 (49), 18154–18165. https://doi.org/10.1021/acs.iecr.1c03615.
Yang, S., Yu, B., Zou, M., Liang, M., 2014. A fractal analysis of laminar flow resistance in roughened microchannels. Int. J. Heat Mass Tran. 77, 208–217. https://doi.org/10.1016/j.ijheatmasstransfer.2014.05.016.
Yang, S., Liang, M., Yu, B., Zou, M., 2015a. Permeability model for fractal porous media with rough surfaces. Microfluid. Nanofluidics 18 (5–6), 1085–1093. https://doi.org/10.1007/s10404-014-1500-1.
Yang, S., Dehghanpour, H., Binazadeh, M., Dong, P., 2017. A molecular dynamics explanation for fast imbibition of oil in organic tight rocks. Fuel 190, 409–419. https://doi.org/10.1016/j.fuel.2016.10.105.
Yang, Y., Yao, J., Wang, C., Ying, G., Song, W., 2015b. New pore space characterization method of shale matrix formation by considering organic and inorganic pores. J. Nat. Gas Sci. Eng. 27 (2), 496–503. https://doi.org/10.1016/j.jngse.2015.08.017.
Yu, B., Li, J., 2004. A geometry model for tortuosity of flow path in porous media. Chin. Phys. Lett. 21 (8), 3. https://doi.org/10.1088/0256-307X/21/8/044.
Yu, B.M., 2005. Fractal character for tortuous streamtubes in porous media. Chin. Phys. Lett. 22 (1), 3. https://doi.org/10.1088/0256-307X/22/1/045.
Zebda, A., Sabbah, H., Ababou-Girard, S., Solal, F., Godet, C., 2008. Surface energy and hybridization studies of amorphous carbon surfaces. Appl. Surf. Sci. 254 (16), 4980–4991. https://doi.org/10.1016/j.apsusc.2008.01.147.
Zeng, Y., Ning, Z., Wang, Q., Sun, H., Huang, L., Ye, H., 2018. Gas transport in self-affine rough microchannels of shale gas reservoir. J. Petrol. Sci. Eng. 167, 716–728. https://doi.org/10.1016/j.petrol.2018.04.045.
Zhang, Q., Su, Y., Wang, W., Lu, M., Sheng, G., 2017. Apparent permeability for liquid transport in nanopores of shale reservoirs: coupling flow enhancement and near wall flow. Int. J. Heat Mass Tran. 115, 224–234. https://doi.org/10.1016/j.ijheatmasstransfer.2017.08.024.
Zhang, T., Javadpour, F., Yin, Y., Li, X., 2020. Upscaling water flow in composite nanoporous shale matrix using lattice Boltzmann method. Water Resour. Res. 56 (4). https://doi.org/10.1029/2019WR026007.
Zhang, T., Li, X., Yin, Y., He, M., Liu, Q., Huang, L., Shi, J., 2019b. The transport behaviors of oil in nanopores and nanoporous media of shale. Fuel 242, 305–315. https://doi.org/10.1016/j.fuel.2019.01.042.
Zhang, W., Feng, Q., Wang, S., Xing, X., 2019a. Oil diffusion in shale nanopores: insight of molecular dynamics simulation. J. Mol. Liq. 290, 111183. https://doi.org/10.1016/j.molliq.2019.111183.
Zhao, S., Hu, Y., Yu, X., Liu, Y., Bai, Z., Liu, H., 2017. Surface wettability effect on fluid transport in nanoscale slit pores. AIChE J. 63 (5), 1704–1714. https://doi.org/10.1002/aic.15535.